Supplementary Information

for

T and V-shaped donor-acceptor fluorophores involving pyridoquinoxaline: large Stokes shift, environment-sensitive tunable emission and temperature-induced fluorochromism

Bahadur Sk, Saurabh Khodia and Abhijit Patra*

Department of Chemistry, Indian Institute of Science Education and Research Bhopal, Bhopal Bypass Road, Bhauri, Bhopal 462066, Madhya Pradesh, India

Email: abhijit@iiserb.ac.in

Contents

I. Materials and methods

1.1 Chemicals:

All chemicals were used as received unless otherwise stated. 9,10-phenanthrenequinone (99%), 3,4-diaminopyridine (99%), *N*-bromosuccinimide (99%), palladium(II) acetate (99.9%), carbazole (99%), cesium carbonate (99%), [1,1'-bis(diphenylphosphino)ferrocene]dichloropalladium(II) complex with dichloromethane, bis(triphenylphosphine)-palladium(II) dichloride (98%), dimethyl sulfoxide (99%), toluene (99.85%), tetrakis(triphenylphosphine)palladium(0) (99.9%) were received from Sigma-Aldrich. Sodium hydroxide (99%), potassium carbonate, acetic acid, concentrated sulphuric acid, 1,4-dioxane, chloroform and hexane were received from Merck. Carbazole (99%), bromine (99%), THF (99%), ethanol (99.8%) from Spectrochem, Tri-tert-butylphosphine (96%) was received from Alfa aesar.

1.2 Instrumentation:

NMR Spectroscopy: ^{1}H and ^{13}C-NMR spectra were recorded on Bruker Avance III 500 and 700 MHz NMR spectrometer and the chemical shifts (δ) are reported in parts per million (ppm) using residual solvent signals as internal standards.

FTIR Spectroscopy: FTIR measurements were carried out on Perkin Elmer FTIR spectrophotometer. Ten scans were signal-averaged, with a resolution of 4 cm^{-1} at room temperature. KBr pellet was used for the measurements.

Matrix-Assisted Laser Desorption Ionization (MALDI-ToF): Matrix-assisted laser desorption ionization time of flight mass spectrometry was performed with Bruker Daltonics UltrafleXtreme, using software flex Control version 3.4.

Steady-state absorption spectroscopy: The UV-Vis absorption spectra were recorded on a Cary 100 spectrophotometer.

Steady-state fluorescence spectroscopy: Steady-state fluorescence measurements were carried out on a Jobin Yvon Horiba Model Fluorolog-3-21.

Time-resolved fluorescence Spectroscopy: Time-resolved fluorescence measurements were carried out using time-correlatedsingle-photon counting (TCSPC) spectrometer (Delta Flex-01-DD/HORIBA). Delta diode laser 339 and 440 nm were used as excitation source. Picosecond photon detection module with photomultiplier tube was used as a detector. The instrument response function was recorded by using an aqueous solution of Ludox. Decay curves were analyzed by nonlinear least-squares iteration using IBH DAS6 (version 6.8) decay analysis software. The quality of the fit was assessed by the fitting parameters (χ^2) as well as the visual inspection of the residuals.

Rheometer: The viscosity measurement was performed in Rheoplus MCR102 (modular compact rheometer, Anton Paar GmbH, Austria-Europe) rheometer using a standard concentric cylinder system (CC27/T200/AL) at 25 °C. The different mixture of glycerol/ methanol solutions was placed in the concentric cylinder and the respective viscosities were measured.

II. Synthesis and Characterization
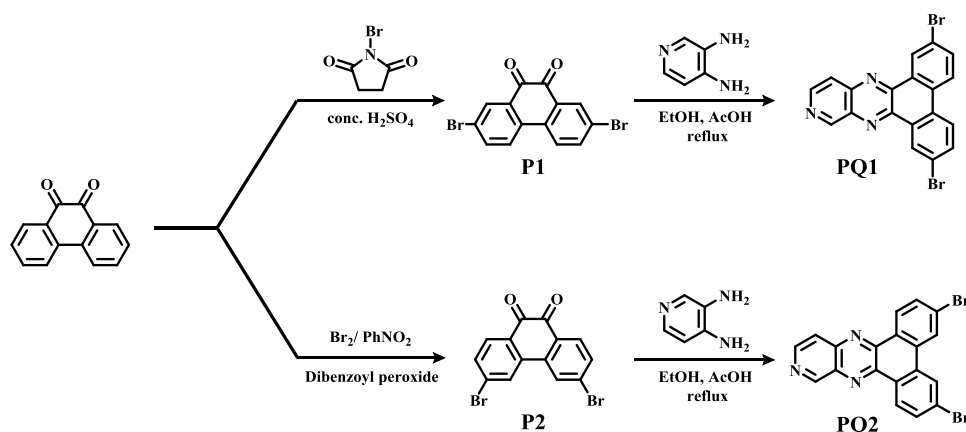
Scheme S1 Synthetic schemes of PQ1 (2,7-dibromodibenzo[f,h]pyrido[3,4-b]quinoxaline) and PQ2 (3,6-dibromodibenzo[f,h]pyrido[3,4-b]quinoxaline).

P1 and P2 were synthesized following a protocol reported earlier.[1, 2] The typical synthesis procedure for PQ1, PQ2, PQCz-T and PQCz-V are given below.

Synthesis of 2,7-dibromophenanthrene-9,10-dione (P1): N-bromosuccinimide (1 g, 2.5 eqv.) was added to a solution of phenanthrene-9,10-dione (500 mg, 1 eqv.) in 98% H_2SO_4 while stirring. The stirring was continued for 3 h at room temperature. The mixture was poured onto crushed ice. The orange product was filtered off, washed with cold water and recrystallized in DMSO (75% yield) to obtain 2,7-dibromophenanthrene-9,10-dione (P1). ^{1}H NMR (500 MHz, DMSO-d_6): δ 8.26 (d, $J = 8.6$ Hz, 2H), 8.09 (d, $J = 2.3$ Hz, 2H), 7.97 (dd, $J = 8.5, 2.3$ Hz, 2H). ^{13}C NMR (126 MHz, DMSO): δc 176.80, 137.43, 133.60, 133.16, 131.03, 126.93, 122.85. MS (MALDI-ToF): Calculated for $C_{14}H_6Br_2O_2[M]^+$: 366.004, found: 366.945 g/mol.

Synthesis of 3,6-dibromophenanthrene-9,10-dione (P2): A mixture of 1g (1 eqv.) of phenanthrene-9,10-quinone, 93 mg (0.08 eqv.) dibenzoyl peroxide and 0.1 mL bromine in 20 mL nitrobenzene was refluxed at 120 °C. After initiation of the reaction (vigorous evolution of HBr gas) additional 0.44 mL of bromine was added dropwise. The reaction mixture was stirred for 5 h at 120 °C and then was allowed to cool to room temperature. The product precipitated out upon addition of hexane. After filtration and washing with copious amounts of hexane 3,6-dibromophenanthrene-9,10-quinone (60% yield) obtained as dark yellow solid (P2). ^{1}H NMR (500 MHz, CDCl$_3$): δ 8.12 (d, $J = 1.9$ Hz, 2H), 8.07 (dd, $J = 8.2, 1.3$ Hz, 2H), 7.76 – 7.54 (m, 2H). ^{13}C NMR (126 MHz, CDCl$_3$): δ 178.75, 135.83, 133.33, 132.00, 131.99, 129.75, 127.29. MS (MALDI-ToF): Calculated for $C_{14}H_6Br_2O_2[M]^+$: 366.004, found: 366.975 g/mol.

Synthesis of 2,7-dibromodibenzo[f,h]pyrido[3,4-b]quinoxaline (PQ1): Diaminopyridine (180 mg, 1 eqv.) and P1 (500 mg, 1 eqv.) were dissolved in ethanol. A catalytic amount of acetic acid was added to the solution. The mixture was refluxed for 5 h. The reaction mixture was brought to room temperature and the filtration followed by washing with ethanol afforded the product as a yellow solid (80% yield). ^{1}H NMR (700 MHz, CDCl$_3$): δ 9.72 (s, 1H), 9.28 (dd, $J = 3.8, 2.1$ Hz, 2H), 8.91 (d, $J =$

5.8 Hz, 1H), 8.19 (dd, J = 8.6, 5.8 Hz, 2H), 8.06 (d, J = 5.8 Hz, 1H), 7.83 (ddd, J = 12.1, 8.6, 2.2 Hz, 2H). ^{13}C NMR (126 MHz, CDCl$_3$): δ 155.31, 146.87, 143.93, 142.39, 136.89, 134.54, 134.05, 129.60, 129.16, 124.52, 124.47, 123.21, 123.07, 121.21. MS (MALDI-ToF): Calculated for C$_{19}$H$_9$Br$_2$N$_3$[M]$^+$: 439.103, found: 439.932 g/mol.

Synthesis of 3,6-dibromodibenzo[f,h]pyrido[3,4-b]quinoxaline (PQ2): Diaminopyridine (180 mg, 1 eqv.) and P2 (500 mg, 1 eqv.) were dissolved in ethanol. The mixture was refluxed for 5 h. The reaction mixture was brought to room temperature and filtration followed by washing with ethanol afforded the product as a yellowish brown solid (74% yield). ^{1}H NMR (500 MHz, CDCl$_3$): δ 9.81 (s, 1H), 9.29 (d, J = 8.6 Hz, 2H), 8.93 (d, J = 5.9 Hz, 1H), 8.65 (dd, J = 3.9, 1.8 Hz, 2H), 8.15 (d, J = 5.9 Hz, 1H), 7.94 (ddd, J = 8.6, 4.9, 1.8 Hz, 2H). ^{13}C NMR (126 MHz, CDCl$_3$): δ 155.25, 155.23, 146.74, 144.68, 143.99, 142.50, 136.91, 134.61, 134.11, 130.99, 130.73, 129.98, 129.65, 129.20, 124.57, 124.52, 123.24, 123.09, 121.30. MS (MALDI-ToF): Calculated for C$_{19}$H$_9$Br$_2$N$_3$[M]$^+$: 439.103, found: 439.974 g/mol.
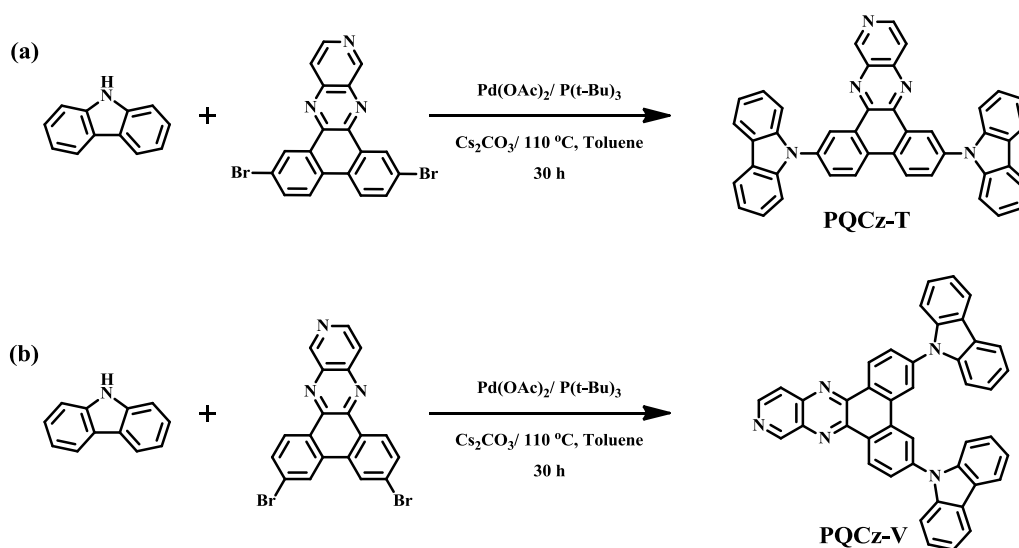
Scheme S2 Schematic representation of synthesis of donor-acceptor systems.

Synthesis of 2,7-di(9H-carbazol-9-yl)dibenzo[f,h]pyrido[3,4-b]quinoxaline (PQCz-T): Toluene (10 mL) was added to a mixture of 2,7-dibromodibenzo[f,h]pyrido[3,4-b]quinoxaline (200 mg, 1 eqv.), 9H-carbazole (1.7 g, 2.2 eqv.), Pd(OAc)$_2$ (5 mg, 0.05 eqv.), Cs$_2$CO$_3$ (600 mg, 2.5 eqv.) and P(t-Bu)$_3$ (9 mg, 0.05 eqv.). The solution was stirred under argon atmosphere at 110 °C for 30 h. The mixture was allowed to cool to room temperature and was quenched by the addition of water. The organic layer was collected and purified by column chromatography (neutral alumina, DCM/Hexane). The compound obtained as red powder (yield 68%). ^{1}H NMR (500 MHz, CDCl$_3$): δ 9.75 (s, 1H), 9.71 (t, J = 2.1 Hz, 2H), 8.87 (d, J = 5.9 Hz, 1H), 8.84 (dd, J = 8.7, 3.5 Hz, 2H), 8.22 (d, J = 7.7 Hz, 4H), 8.13 (td, J = 8.7, 2.3 Hz, 2H), 8.08 (d, J = 6.0 Hz, 1H), 7.64 – 7.60 (m, 4H), 7.49 (t, J = 7.6 Hz, 4H), 7.37 (t, J = 7.3 Hz, 4H). ^{13}C NMR (126 MHz, CDCl$_3$): δ 155.43, 146.76, 144.19, 140.76, 138.17, 138.04, 137.16, 131.62, 131.35, 131.22, 130.48, 130.19, 129.67, 126.25, 125.14, 124.61, 123.77, 121.35, 120.54, 120.48, 109.76. MS (HRMS-ESI): Calculated for C$_{43}$H$_{25}$N$_5$[M+H]$^+$: 612.218, found: 612.2154 g/mol.

Synthesis of 3,6-di(9H-carbazol-9-yl)dibenzo[f,h]pyrido[3,4-b]quinoxaline (PQCz-V): Similar synthetic approach as that of PQCz-T was adopted for the synthesis of PQCz-V. The crude compound was purified by column chromatography (neutral alumina, DCM/Hexane). The desired compound was obtained as orange solid (yield 72%). ^{1}H NMR (500 MHz, CDCl$_3$): δ 9.90 (s, 1H), 9.73 (d, J = 8.5 Hz, 2H), 8.99 (d, J = 5.9 Hz, 1H), 8.74 (dd, J = 4.6, 1.8 Hz, 2H), 8.24 (d, J = 5.8 Hz, 1H), 8.19 (d, J = 7.8 Hz, 4H), 8.10 (ddd, J = 8.5, 4.1, 1.9 Hz, 2H), 7.62 (d, J = 8.3 Hz, 4H), 7.46 (t, J = 7.6 Hz, 4H), 7.35 (t, J = 7.4 Hz, 4H). ^{13}C NMR (126 MHz, CDCl$_3$): δ 155.35, 146.75, 145.73, 144.27, 141.31, 140.82, 140.48, 140.42, 137.26, 133.96, 133.22, 129.37, 128.87, 128.86, 128.52, 127.32, 127.14, 126.39, 126.37, 123.92, 123.91, 121.39, 120.99, 120.96, 120.75, 120.69, 120.59, 120.59, 109.62. MS (MALDI-ToF): Calculated for C$_{43}$H$_{25}$N$_5$[M+H]$^+$: 612.215, found: 612.247 g/mol.

III. Spectroscopic characterization
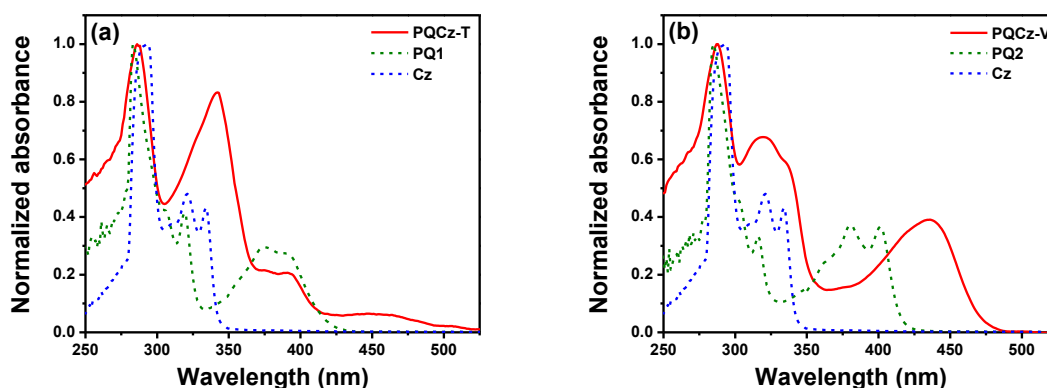
3.1 Electronic absorption

Figure S1 Normalized absorption spectra of (a) PQCz-T and (b) PQCz-V compared with absorption of the respective acceptor (PQ1 and PQ2) and donor (Cz) in toluene.

The absorption spectra of PQCz-T and PQCz-V were compared with that of their constituent units (donor and acceptor). The major absorption peak is arising because of the donor carbazole while a hump can be seen at the acceptor (PQ) absorption maximum (Figure S1). The shoulder peaks at 370 and 390 nm in PQCz-T arise due to the PQ1 moiety (Figure S1a). These peaks disappear in PQCz-V leading to a red-shifted absorption band at 430 nm due to the extended conjugation between Cz and PQ2. The similar band around 430 nm is broad and less intense in PQCz-T.

Steady-state absorption measurements of PQCz-T and PQCz-V were carried out in five different solvents of varying polarity. Figure S2 shows the absorption spectra of both the D-A-D systems with no significant change in spectra with varying solvent polarity from toluene to DCM.
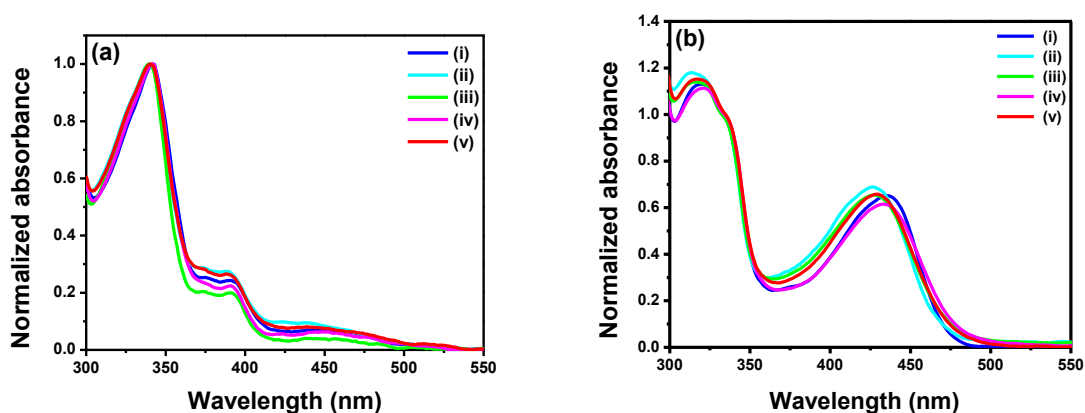

Figure S2 Normalized absorption spectra of (a) PQCz-T and (b) PQCz-V in different solvents: (i) toluene, (ii) 1,4-dioxane, (iii) tetrahydrofuran, (iv) chloroform and (v) dichloromethane.
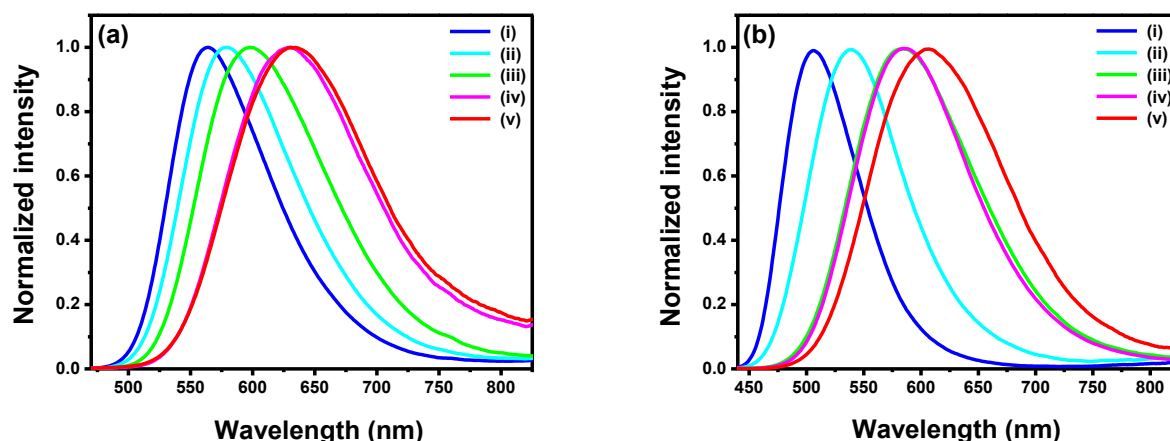
3.2 Steady-state fluorescence

Figure S3 Normalized fluorescence spectra of (a) PQCz-T and (b) PQCz-V in different solvents: (i) toluene, (ii) 1,4-dioxane, (iii) tetrahydrofuran, (iv) chloroform and (v) dichloromethane.

Emission spectra of both the D-A-D compounds are gradually red shifted with increasing solvent polarity depicting highly sensitive solvatochromic behaviour.
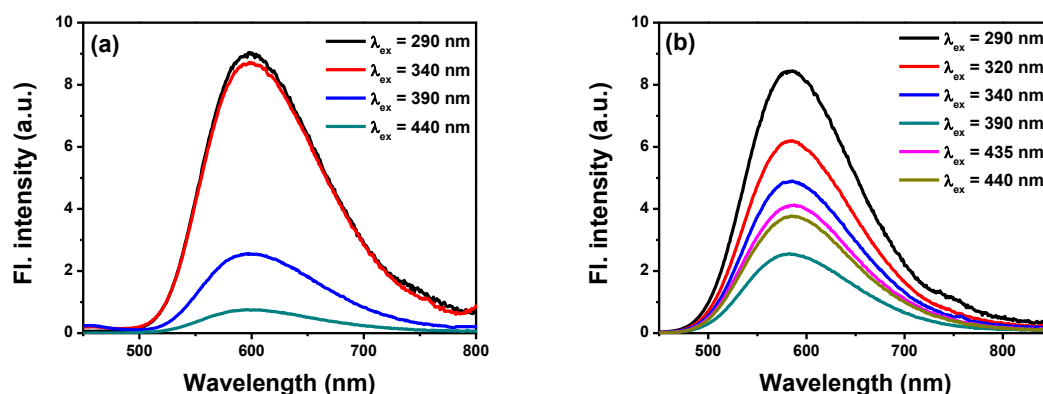

Figure S4 PL spectra of (a) PQCz-T and (b) PQCz-V in THF at different excitation wavelengths.

The emission spectra recorded by exciting at different wavelengths suggested that the emission is independent of the excitation wavelength (Figure S4). It signifies that emission is coming from the same energy state irrespective of excitation wavelengths. Further excitation spectra were recorded with varying solvent polarity at respective emission maxima in different solvents. As shown in Figure S5 excitation spectra are found to be similar to the corresponding absorption and remain unchanged with varying solvent polarity.
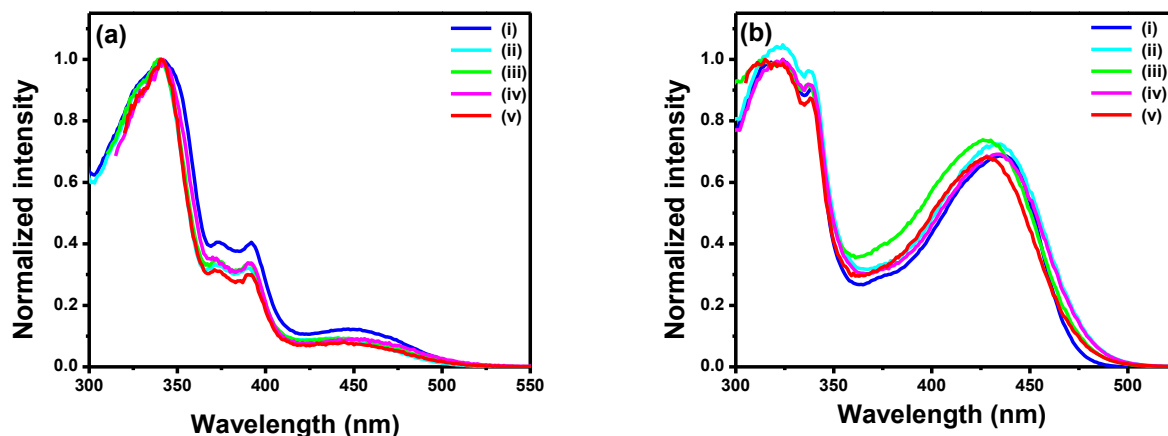
Figure S5 Normalized excitation spectra of (a) PQCz-T and (b) PQCz-V in different solvents: (i) toluene, (ii) 1,4-dioxane, (iii) tetrahydrofuran, (iv) chloroform and (v) dichloromethane.

3.3 PQCz-T vs PQCz-V

The increase in polarity of the excited state due to the large charge separation from donor to acceptor makes the entire D-A-D system highly environment sensitive. Table S1 represents the change of Stokes shift from nonpolar toluene to polar dichloromethane. An obvious red shift in emission maxima was observed from toluene to dichloromethane for both T and V-shaped compounds. A comparative study was done to analyze the relative behaviour of the compounds.

Table S1 Spectroscopic data of the compounds in toluene and dichloromethane.

S. No.	Entry	λ_{abs} (nm)		$\lambda_{em (max)}$ (nm)		Stokes shift (nm)[#]	
		Toluene	DCM	Toluene	DCM	Toluene	DCM
1	PQCz-T	341, 440	341, 440	565	635	125	195
2	PQCz-V	339, 434	339, 430	506	605	72	175

[#] Stokes shift with respect to longer wavelength absorption band.

On comparing both T and V-shaped compounds, it was found that PQCz-T always possess larger Stokes shift in each solvent as compared to PQCz-V. In toluene, PQCz-T accounts for 125 nm shift while PQCz-V shows a lower Stokes shift of 72 nm. As we move from nonpolar to a polar solvent, there is an obvious increase in Stokes shift for both the compounds. In dichloromethane PQCz-T possesses Stokes shift of 195 nm and the same in PQCz-V is 175 nm. Considering the main absorption band at 340 nm in PQCz-T (weak absorption at 440 nm), the Stokes shift would be even larger compared to PQCz-V. The interactions between fluorophores and solvents were studied and were modeled employing the Lippert-Mataga equation for a detailed interpretation of fluorescence emission spectra.[3]

The difference in ICT characteristics leads to the variation of photophysical properties of PQCz-T and PQCz-V. As discussed in the main text (Figure 2), the ground state HOMO of PQCz-T is mainly located on the donor Cz unit and extended to the phenanthrene unit. Whereas, the HOMO is distributed throughout the molecule for PQCz-V. The LUMOs of both the compounds are located on the PQ unit. These HOMO orbital pictures of both the compounds indicate that in PQCz-T, D and A are decoupled whereas, in PQCz-V, D and A are coupled. The intense longer wavelength absorption peak in PQCz-V around 430 nm compared to that of PQCz-T also support the same. The photo-induced charge transfer process is highly dependent on the charge separation and the energy gap between the HOMO and LUMO level.[4, 5] The intramolecular charge transfer also dependent on the linkage position and the geometry of the donor-acceptor.[6-8]

The geometry of both the two compounds are different (T and V-shaped). Donor Cz in PQCz-V is attached to 3 and 6-positions of phenanthrene unit which is *para* with respect to the acceptor pyridoquinoxaline moiety. The facile resonance from Cz to pyridoquinoxaline unit in *p*-substituted PQCz-V is likely to develop a partial double bond character between Cz and PQ unit. Thus, the molecular framework in PQCz-V is relatively rigid due to extended conjugation. On the other hand, donor Cz in PQCz-T is attached to 2 and 7-positions of phenanthrene unit which is *meta* with respect to the acceptor pyridoquinoxaline moiety. Thus, the carbazole units are amenable to free rotation across the D-A linkage in PQCz-T and the molecular framework is relatively flexible.

3.4 Solvatochromism

The solvatochromism refers to the dependence of the absorption or emission color of a fluorophore on the solvent polarity. The solvent-dependent shifts in the fluorescence maxima of the molecules can be mainly attributed to the dipole–dipole interactions between the fluorophore and the solvent. Generally, the blue shift with the increasing solvent polarity is termed as the negative solvatochromism, which occurs because of the more stabilized ground state. The positive solvatochromism is observed when there is a red shift in emission with the increasing solvent polarity.[9] This is because of the stabilized excited state. The Lippert-Mataga (L-M) theory describes the solvent dependence spectral shifts as given in Eq. 1. In this theory, specific solvent-fluorophore interactions, such as hydrogen-bonding are not included.

$$\Delta v = \bar{v}_a - \bar{v}_f = \frac{2}{hc}\left(\frac{\varepsilon - 1}{2\varepsilon + 1} - \frac{n^2 - 1}{2n^2 + 1}\right)\frac{(\mu_E - \mu_G)^2}{a^3} + constant \quad .... (1)$$

$$\text{where:} \quad \bar{v}_a = \frac{1}{\lambda_{abs}^{max}} \, , \quad \bar{v}_f = \frac{1}{\lambda_{em}^{max}} \quad and \quad \Delta f = \left(\frac{\varepsilon - 1}{2\varepsilon + 1} - \frac{n^2 - 1}{2n^2 + 1}\right) \quad .... (2)$$

Eq. 1 shows Stokes shift ($\Delta\bar{v}$) depends on the dipole moments of the fluorophore in the ground (μ_G) and the excited (μ_E) state, respectively. It also depends on the dielectric constant (ε) and the

refractive index (η) of the corresponding solvent. $\bar{v}_a$ and $\bar{v}_f$ represent the wavenumbers of the absorption and the fluorescence emission respectively, h is the Planck's constant, c is the speed of light in vacuum, and a is the Onsager radius of the cavity in which the fluorophore resides. Δf is the orientation polarizability of the solvent (Eq. 2). Plotting the Stokes shift as a function of the orientation polarizability of the solvents gives the Lippert-Mataga plot (Figure S6).[3]

A relation between solvent polarity parameter E_T^N and Stokes shift ($\Delta\bar{v}$) were also established. To define the solvent polarity $E_T(30)$ / E_T^N scale is used.[9] $E_T(30)$ is defined as molar electronic transition energies (E_T) of dissolved pyridinium N-phenolate betaine dye measured in kcal mol^{-1} at room temperature (25 °C) and normal pressure (1 bar).

$$E_T(30)(Kcal\ mol^{-1}) = hc\bar{v}_{max}N_A \ ....\ (3)$$

where h is the Plank's constant, c is the speed of light, N_A is Avogadro's number, and v is the electronic transition energy in wavenumber. E_T^N is the normalized value for which water and tetramethylsilane (TMS) are used as extreme polar and non polar reference solvents, respectively. The normalized E_T^N value is scaled approximately from 0 for TMS, the least polar solvent to 1.000 for water, the most polar solvent.

$$E_T^N = \left(\frac{E_T(solvent) - E_T(TMS)}{E_T(water) - E_T(TMS)}\right) \ ....\ (4)$$

Table S2 Solvent polarity parameters $E_T(30)$/ E_T^N, dielectric constants (ε), refractive indices (η), orientation polarizabilities (Δf) of different solvents and the Stokes shift ($\Delta\bar{v}$) of PQCz-T and PQCz-V as a function of different solvents are shown.

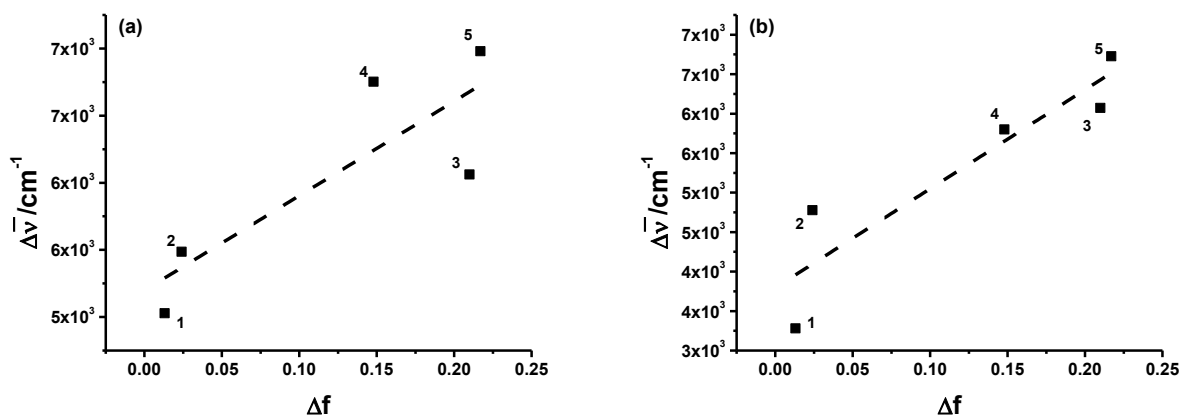| Solvents						Stokes shift $\Delta\bar{v}$ (cm^{-1})	
Entry	$E_T(30)$ **[kcal mol^{-1}]**	E_T^N	ε	η	Δf	**PQCz-T**	**PQCz-V**
Toluene	33.9	0.099	2.38	1.497	0.013	5028	3279
1,4-Dioxane	36.0	0.164	2.25	1.422	0.024	5486	4777
THF	37.4	0.207	7.58	1.407	0.210	6061	6073
Chloroform	39.1	0.259	4.81	1.446	0.148	6753	5800
DCM	40.7	0.309	8.93	1.424	0.217	6979	6727

Figure S6 Lippert-Mataga plot depicting Stokes shift ($\Delta\overline{v}$)versus the solvent orientation polarizability (Δf) of (a) PQCz-T and (b) PQCz-V. The numbers refer to the solvents: (1) toluene, (2) 1,4-dioxane, (3) tetrahydrofuran, (4) chloroform and (5) dichloromethane. The dashed line represents the best linear fit to the data points.

Lippert–Mataga (L-M) plots show nonlinear dependence of the Stokes shift with the Onsager solvent parameter Δf for PQCzs. However, the emission spectral analysis reveals that the PQCz-T shows large red-shifted emission in polar solvents. A relation between solvent polarity parameter E_T^N and Stokes shift ($\Delta\overline{v}$) were also established. A linear relation was obtained for Stokes shift versus solvent polarity as shown in Figure S7.
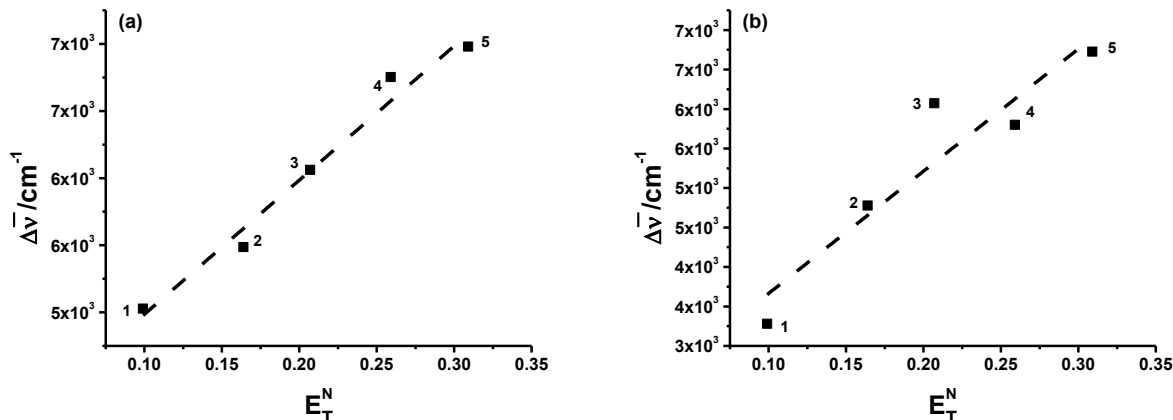

Figure S7 Reichardt's plot depicting Stokes shift ($\Delta\overline{v}$) of (a) PQCz-T and (b) PQCz-V as a function of the solvent polarity parameter E_T^N. The numbers refer to the solvents: (1) toluene, (2) 1,4-dioxane, (3) tetrahydrofuran, (4) chloroform and (5) dichloromethane. The straight line represents the best linear fit to the data points.

3.5 Fluorescence quantum yield and lifetime measurements

The fluorescence quantum yields of PQCz-T was estimated by comparison with quinine hemisulfate dye in water (Φ_f = 59%). The quantum yield of PQCz-V was calculated using coumarin 153 in ethanol (Φ_f = 54.4%).[10, 11]

$$\Phi_{f,x} = \Phi_{f,s} * \frac{F_X}{F_S} * \frac{f_S}{f_X} * \frac{n_X^2}{n_S^2} \dots (5)$$

Where Φ_f is the fluorescence quantum yield, the subscript x denotes sample, and the subscript s refers to the standard. F denotes integral fluorescence, n refers to the refractive index of the solvent used in the measurements and f is the absorption factor at the excitation wavelength given by the following equation: $f = 1 - 10^{-\varepsilon(\lambda_{ex})cl} = 1 - 10^{-A(\lambda_{ex})}$, Where A is the absorbance and ε = molar extinction coefficient in L mol^{-1} cm^{-1}.

The absolute photoluminescence quantum yield (PLQY) of PQCz solid powder was measured using Fluorolog-3-21 spectrophotometer equipped with a BaSO$_4$-coated calibrated integrating sphere, Model F-3029, Quanta-Phi 6 (Jobin Yvon Horiba). The quantum yields were estimated taking the average of three measurements and the reported values are within the error of ± 2%.
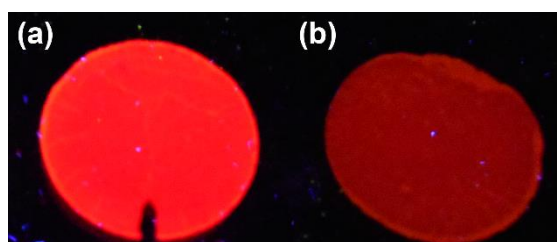

Figure S8 Digital photographs of (a) PQCz-T and (b) PQCz-V in the form of KBr pellets under the illumination of 365 nm UV light.
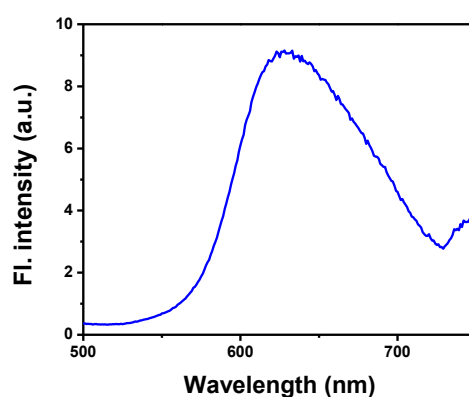

Figure S9 The solid state emission (λ_{ex} = 340 nm) spectrum of PQCz-T.

Table S3 Solid state fluorescence quantum yields of PQCz-T and PQCz-V.

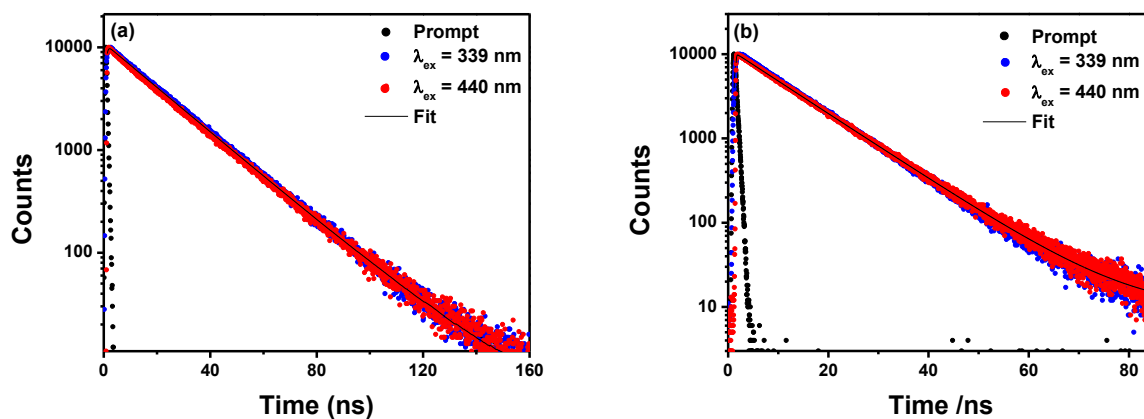| Compound	Solid state Φ_f(%)
PQCz-T	10
PQCz-V	1.5

Figure S10 Fluorescence decay profiles of (a) PQCz-T (λ_{em} = 600 nm) and (b) PQCz-V (λ_{em} = 580 nm) in tetrahydrofuran at different excitation wavelengths. The continuous black lines are the exponential fit to the decay curves.

Table S4 Fluorescence decay parameters of PQCz-T and PQCz-V in tetrahydrofuran at different excitation wavelengths; lifetime monitored at respective emission maxima and the quality of fitting (χ^2) are shown.

Compound	λ_{ex} (nm)	λ_{em} (nm)	Lifetime (ns)	
			$\tau^{\#}$	χ^2
PQCz-T	339	600	20.0	1.14
	440	600	20.3	1.08
PQCz-V	339	580	10.8	1.09
	440	580	11.2	1.07

[#]It is evident that the fluorescence lifetime remains independent with respect to the excitation wavelengths.
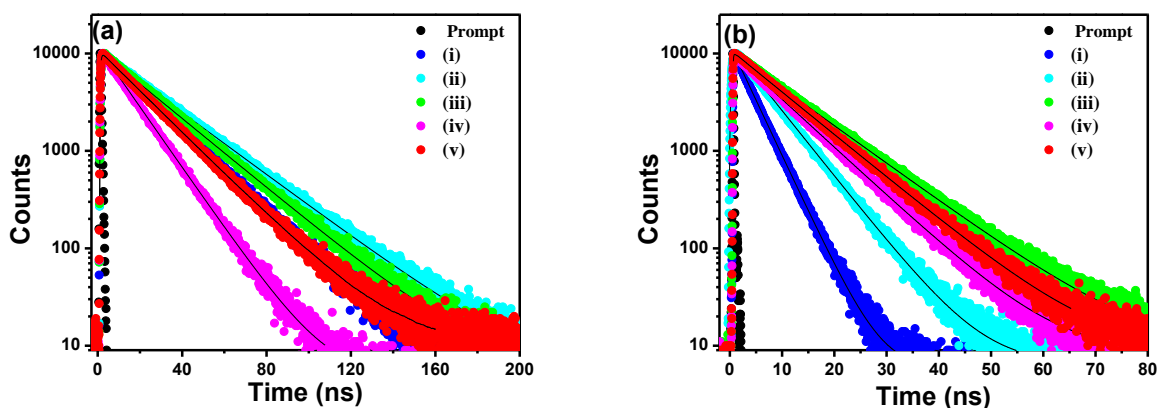

Figure S11 Fluorescence decay profiles (λ_{ex} = 339 nm) of (a) PQCz-T and (b) PQCz-V in: (i) toluene, (ii) 1,4-dioxane (iii) tetrahydrofuran, (iv) chloroform and (v) dichloromethane. The continuous black lines are the exponential fit to the decay curves.

3.6 Spectroscopic data tables:

Table S5 Spectroscopic data of PQCz-T in various organic solvents; lifetime monitored at respective emission maxima and the quality of fitting (χ^2) are shown.

Solvent		Absorption	Fluorescence	Quantum Yield	Stokes shift	Lifetime (ns)	
Entry	E_T^N	λ_{max} (nm)	λ_{max} (nm)	%	(nm)	$\lambda_{ex} = 339$ nm	(χ^2)
Toluene	0.099	341, 440	565	28	125	21.0	1.07
Dioxane	0.164	340, 440	580	21	140	27.2	1.08
THF	0.207	341, 440	600	16	160	24.4	1.12
CHCl$_3$	0.259	342, 440	626	9	186	13.7	1.08
DCM	0.309	341, 440	635	11	195	20.3	1.04

Table S6 Spectroscopic data of PQCz-V in various organic solvents; lifetime monitored at respective emission maxima and the quality of fitting (χ^2) are shown.

Solvent		Absorption	Fluorescence	Quantum Yield	Stokes shift	Lifetime (ns)	
Entry	E_T^N	λ_{max} (nm)	λ_{max} (nm)	%	(nm)	$\lambda_{ex} = 339$ nm	(χ^2)
Toluene	0.099	339, 434	506	50	72	3.8	1.07
Dioxane	0.164	338, 428	538	52	110	6.4	1.12
THF	0.207	338, 430	582	49	152	11	1.07
CHCl$_3$	0.259	339, 434	580	35	146	8.8	1.05
DCM	0.309	339, 430	605	33	175	10	1.00

IV. Viscosity-induced fluorescence enhancement

Preparation of different viscous solutions:

A series of viscous solutions was prepared by mixing methanol and glycerol following a reported procedure.[12] A stock solution of PQCz-T in chloroform (4×10^{-4} M) was prepared. 50 µL of the $CHCl_3$ solution was added to the mixture of glycerol and methanol of definite proportion so as to make the total volume of the solution 4 mL. The viscosity (η_{mix}) of the resultant solution (5×10^{-6} M) was calculated with the following equation.[12]

$$ln\,\eta_{mix} = \sum_i w_i ln\,\eta_i \quad .... \quad (6)$$

where w_i is the volume fraction and η_i is the viscosity of the ith solvent. The calculated value was also further verified by Rheometry and the error limits were found to be ±1.5, ±4 and ±8 from 0.6-16 cP, 24-72 cP and 104-454 cP, respectively.

Table S7 The viscosity of the solutions with increasing percentage of glycerol.

Percentage (%)	η_{mix} (cP)		Percentage (%)	η_{mix} (cP)
0	0.6		50	24
5	0.8		55	34
10	1.2		60	50
15	1.8		65	72
20	3		70	104
25	4		75	151
30	5		80	218
35	8		85	315
40	11		90	454
45	16		-	-

Absorptions of PQCz-T and PQCz-V were found to be mostly unaffected with the change in viscosity of the medium (Figure S12). PQCz-T is non-fluorescent in methanol due to the nonradiative deactivation in polar protic solvents. The fluorescence intensity increases drastically with increasing solvent viscosity from 11 to 454 cP using glycerol/methanol mixture (Figure 3a, main text). The dielectric constant of methanol ($\varepsilon = 33$) and glycerol ($\varepsilon = 42$) are different. Thus, with increasing the % of glycerol there will be a slight increment of solvent polarity.[13] But, if only polarity factor is dominated then it would quench the fluorescence at higher % of glycerol. We would also expect drastic red-shifted emission peak with increasing polarity (as evidenced by the solvatochromic studies demonstrated in the main text, Figure 1). But with the increasing percentage of glycerol only slight blue shift was observed with a drastic enhancement of fluorescence intensity (Figure 3). This observation indicates that in the presence of steric environment, the polarity effect is likely to be less pertinent. The restriction of the molecular rotation hinders the lower energy deactivation pathways (TICT) upon increasing the viscosity of the medium. It results in enhancement of fluorescence. Consequently, the rigidification of molecular geometry leads to a slight blue shift in emission with increasing viscosity.
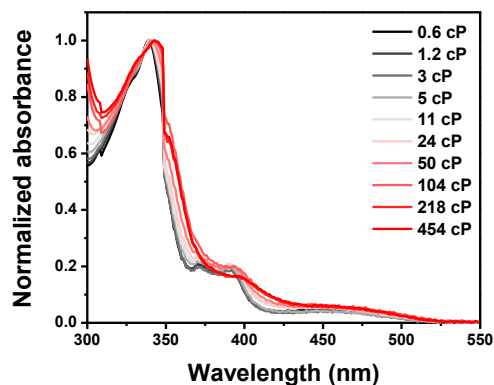
Figure S12 Normalized absorption spectra of PQCz-T in solutions of varying viscosities.

The viscosity dependent-fluorescence of PQCz-T was analyzed using the Förster–Hoffmann theory as per the following equation.[12]

$$log I = C + x log \eta \qquad (7)$$

where η is the viscosity of the medium, C is a constant depending on the experimental parameters and x is the viscosity sensitivity of the molecular rotors. The fluorescence intensity (I) of PQCz-T exhibits a nearly linear relationship at the intermediate range of viscosities (Figure S13). On the other hand, there was no significant enhancement of fluorescence intensity of PQCz-V with increasing solution viscosity (Figure S14). The decay profiles also corroborate the same fact (Figure S15, Table S8).
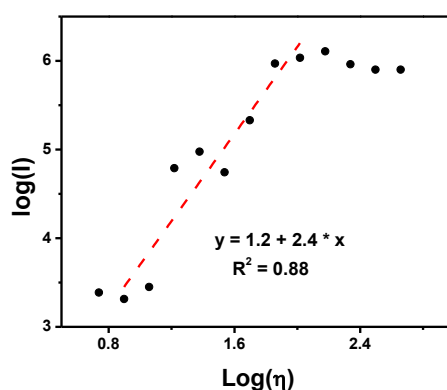
Figure S13 The double logarithmic plot of fluorescence intensity (λ_{em} = 635 nm) and viscosity of the solutions of PQCz-T in glycerol/ methanol mixture.
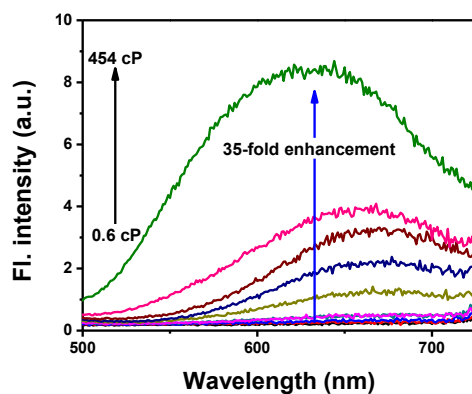
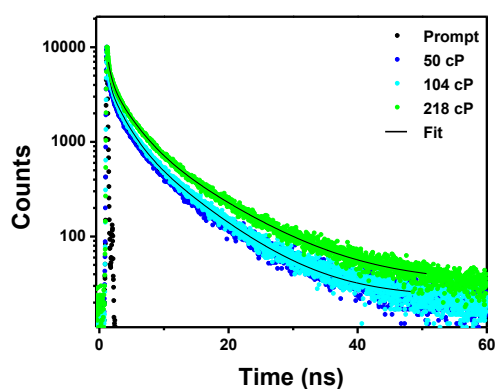**Figure S14** Emission spectra (λ_{ex} = 340 nm) of PQCz-V in solution of varying viscosities.

Figure S15 Fluorescence decay profiles (λ_{ex} = 440 nm, λ_{em} = 640 nm) of PQCz-V in solution of varying viscosities.

Table S8 Fluorescence decay parameters of PQCz-V at medium of different viscosities (λ_{ex} = 440 nm, λ_{em} = 640 nm); the decay times (τ_1, τ_2, and τ_3) and the respective fractional contributions (α_1, α_2 and α_3), the amplitude average decay time (τ_{avg}) and the quality of fitting (χ^2) are shown.

Viscosity (cP)	Lifetime (ns)							
	τ_1	α_1	τ_2	α_2	τ_3	α_3	τ_{avg}	χ^2
50	0.5	8.1	2.7	39.5	8.9	52.4	5.7	1.10
104	0.3	8.8	2.2	35.7	7.8	55.5	5.1	1.17
218	0.5	7.0	2.8	37.8	9.6	55.2	6.3	1.06

The amplitude average fluorescence decay time of PQCz-T also increases from 23.7 ns to 26.6 ns with increasing the solution viscosity from 24 cP to 454 cP (Figure S16, Table S9). The rotation of the C–N bond between PQ unit and Cz is restricted in a highly viscous medium. The prevention of the nonradiative dissipation of the excited state energy through the rotation leads to strong emission. PQCz-T exhibits a single exponential fluorescence decay profile (i.e., one relaxation pathway) in different solvents and bi-exponential decay in the low viscosity range under 24 cP. It shows a tri-exponential fluorescence decay profile (i.e., three relaxation pathways) in the range of high viscosity.

17

Such complex decay profiles indicate multiple emissive species originated due to the presence of two different rotational donor (Cz) groups.

Kwon and coworkers interpreted the biexponential decay profiles of pyrrolic molecular rotors in the high viscous medium as originated from different rotational isomers.[14] The scenario in PQCz-T would be even more complex due to the presence of two donor groups. The rotation of two carbazole units could be different depending on the change in twist angle upon increasing the viscosity of the medium. As shown in Table S9, the fastest component with decay time 4-6 ns with amplitude < 10% can be attributed to the one rotamer. This component is absent in the low viscosity range under 24 cP. The decay time of the slowest component increases with increasing solution viscosity from 30 to 42 ns. This longer component can be ascribed to another rotamer. The third component with the decay time in the range of 12-20 ns is similar to that observed in organic solvents.
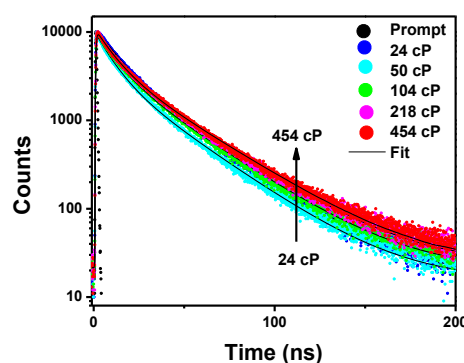

Figure S16 Fluorescence decay profiles (λ_{ex} = 339 nm, λ_{em} = 635 nm) of PQCz-T in solution of varying viscosities.

Table S9 Fluorescence decay parameters of PQCz-T at medium of different viscosities (λ_{ex} = 339 nm, λ_{em} = 635 nm); the decay times (τ_1, τ_2 and τ_3) and the respective fractional contributions (α_1, α_2 and α_3), the amplitude average decay time (τ_{avg}) and the quality of fitting (χ^2) are shown.

Viscosity (cP)	Lifetime (ns)							
	τ_1	α_1	τ_2	α_2	τ_3	α_3	τ_{avg}	χ^2
24	-	-	12.2	38.9	31.0	61.1	23.7	1.14
50	4.1	8.5	16.7	51.7	37.6	39.7	23.9	1.09
104	4.9	8.8	18.3	50.9	39.2	40.2	25.5	1.06
218	5.3	8.6	18.8	48.0	40.0	43.4	26.8	1.06
454	5.9	9.9	20.3	50.4	42.2	39.6	27.5	1.09

Time-resolved fluorescence anisotropy (TRFA):

The rotational Brownian motion of the molecule as a whole is slowed down in the medium of high viscosity. The rotational diffusion rate can be determined using polarization-resolved TCSPC. Time-resolved fluorescence anisotropy (TRFA) measurements were carried out by collecting repeated sequences of 40 s vertical (parallel) and 40 s horizontal (perpendicular) polarized fluorescence

emission. The measurement was carried out until the difference of fluorescence counts reached ~5000. The time-dependent fluorescence anisotropy values r(t) were calculated using the following expression:

$$r(t) = \frac{I_{\parallel}(t) - GI_{\perp}(t)}{I_{\parallel}(t) + 2GI_{\perp}(t)} \quad \dots\dots\dots\dots\dots (8)$$

where $I_{\parallel}(t)$ and $I_{\perp}(t)$ are the vertically and horizontally polarized components of probe emission with the excitation by the respective polarized light. G defines the instrumental correction factor (polarization characteristics of the photometric system).

The anisotropy decay considering freely rotating spherically symmetric molecules as a function of time is depicted according to the following equation:

$$r(t) = r_0 e^{-\frac{t}{\tau_r}} \quad \dots\dots\dots\dots (9)$$

where r_0 is the limiting anisotropy, which is the anisotropy value just after photoexcitation (i.e., at t = 0) and τ_r is the rotational correlation time, which is a parameter of molecular rotation.[15] The single exponential anisotropy decay of PQCz-T in chloroform (0.5 cP) with short rotational correlation time (τ_r) become biexponential with very high amplitude average rotational correlation time ($\tau_{avg,r}$) at 80% glycerol/ methanol mixture (Figure S17, Table S10). The increase in the rotational correlation time is due to the restriction of molecular motions in the medium of high viscosity.[16, 17]
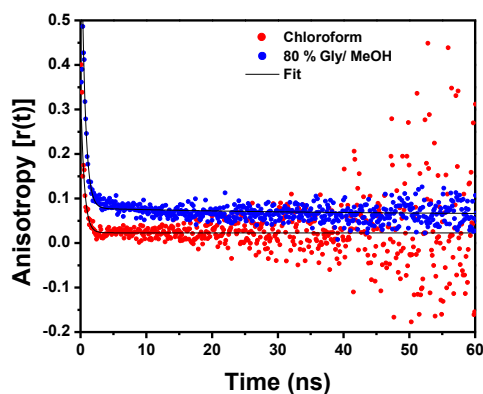

Figure S17 Time-resolved fluorescence anisotropy decay profiles of PQCz-T in chloroform and in 80% glycerol/ methanol mixture (218 cP).

Table S10 Time-resolved fluorescence anisotropy decay parameters of PQCz-T in chloroform and in 80% glycerol/ methanol mixture (λ_{ex} = 339 nm, λ_{em} = 640 nm); the rotational correlation times (τ_{1r} and τ_{2r}) and the respective fractional contributions (α_1 and α_2) and the amplitude average rotational correlation time ($\tau_{avg, r}$) are shown.

Viscosity of the medium	Lifetime (ns)				
	τ_{1r}	τ_{2r}	α_1	α_2	$\tau_{avg, r}$
0.5 cP	0.5	-	100	-	-
218 cP	0.5	36.8	38.58	61.42	22.7

V. Temperature-induced tunable fluorescence

The temperature-dependent fluorescence measurements were carried out in quartz cuvettes of 1 cm path length, fitted in a cuvette holder thermally equilibrated using a Newport Peltier thermostat (Newport Corporation, USA, Model No. 350B). Measurements were performed in the temperature range of -10 – 65 °C. The temperature was further verified with a IR thermometer before and after taking the emission spectra. The variation of temperature for each measurement was within ±2 °C.

PQCz-T in THF exhibits dramatic thermochromic behaviour leads to temperature-induced tunable fluorescence from orange-red to blue including a single component near white-light emission (Figure 4, main text). The dramatic fluorochromism can be attributed to the subtle variation of structural change as discussed in the following section. Interestingly, there was no change in absorption spectra with the variation of temperature ruling out any possibility of degradation of the compound (Figure S18). We performed concentration dependent fluorescence measurements of PQCz-T in THF to probe any possible effect of aggregation. There was no change in the shape and peak maxima with increasing the concentration from 1 μM to 25 μM (Figure S19). The enhancement of fluorescence intensity with concentration is simply the effect of increasing optical density. Thus, the observed tunable emission is not due to the aggregation-deaggregation effect of PQCz-T with the variation of temperature. The temperature-induced fluorochromism was also observed in other solvents, like chloroform. Unlike the wide variation of fluorescence color as noticeable in THF, ~ 40 nm blue shift and the enhancement of intensity of emission was detected with the increasing temperature in more polar solvent chloroform (Figure S20). We carried out the same experiment in a high boiling solvent, like toluene (Figure S21). Similar to the response observed in chloroform, the slight blue shift is noticeable with increasing temperature which can be accounted due to the decrease of the polarity of the medium (*vide infra*). There was no significant effect of temperature on fluorescence in PQCz-V (Figure S22).

Figure 4b in the main text was prepared by capturing the images under the irradiation of 365 nm UV light. PQCz-T in THF (5 μM) was digested at respective temperature for 10 minutes. It was observed that the change in fluorescence color was even faster in the presence of irradiation of light. The linear plot in Figure 4d was obtained by fitting the ratio of fluorescence intensity at 415 and 610 nm in the range of 263 to 330 K. The goodness of the fit (R^2) is found to be 0.99 indicating a good linear relationship between the ratio of fluorescence intensity and the absolute temperature. The fitted equation is given below

$$\left(\frac{I_{415}}{I_{415} + I_{610}}\right) = 0.0065 \times T - 1.727 \quad \ldots\ldots\ldots\ldots (10)$$

where I_{415} and I_{615} is the fluorescence intensity at the emission wavelength 415 and 610 nm, respectively. The slope of the best linear fit is 0.0065 K^{-1} or 0.65% K^{-1}. It indicates that a short range of temperature can be measured precisely.
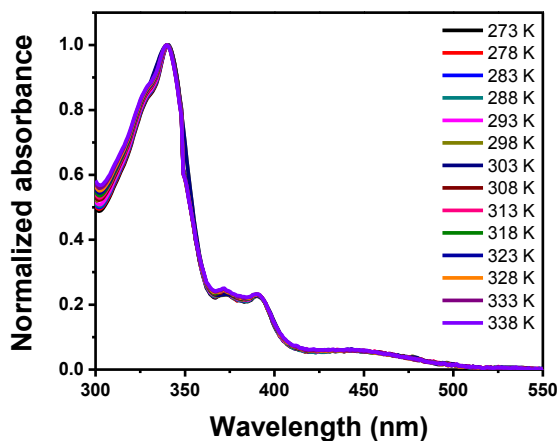

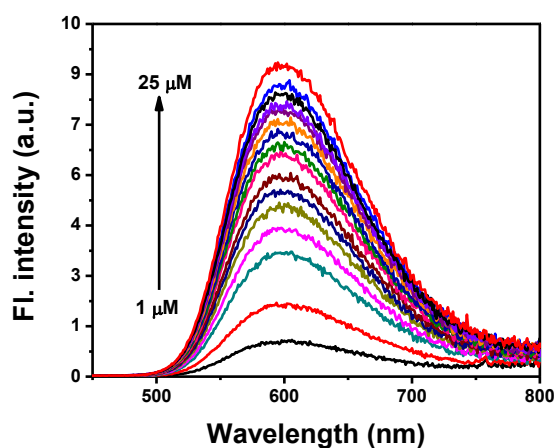**Figure S18** Normalized absorption spectra of PQCz-T at different temperature in THF.

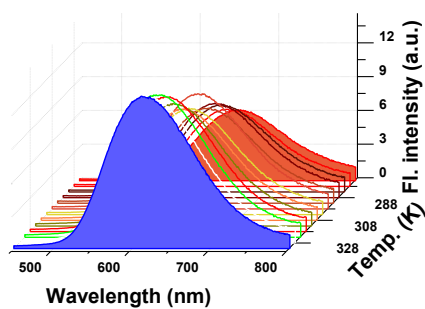**Figure S19** The concentration-dependent emission spectra (λ_{ex} = 340 nm) of PQCz-T in THF.

Figure S20 Emission spectra (λ_{ex} = 340 nm) of PQCz-T in chloroform (5 μM) at different temperatures.
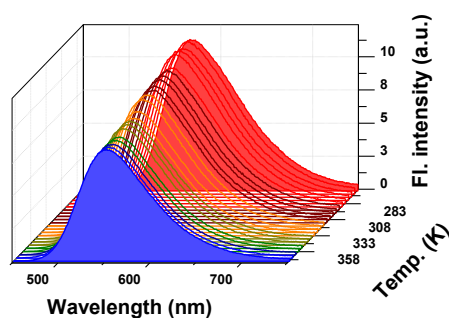
Figure S21 Fluorescence spectra (λ_{ex} = 340 nm) of PQCz-T in toluene (5 μM) at different temperatures (263 K to 373 K).
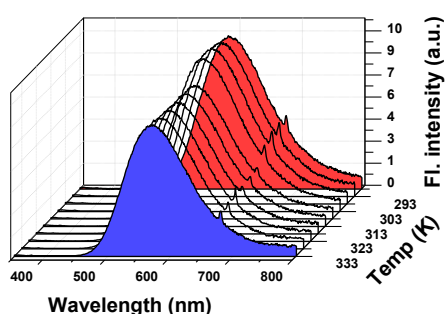
Figure S22 The emission spectra (λ_{ex} = 340 nm) of PQCz-V in THF (5 μM) at different temperatures.

The time-resolved fluorescence measurements (λ_{ex} = 339 nm) of the final blue emitting solution of PQCz-T obtained after the cooling-heating-cooling cycle indicate a multi-exponential decay (Figure S23, Table S11). PQCz-T exhibits a single exponential fluorescence decay in different solvents at room temperature. After a cooling-heating-cooling cycle in THF, PQCz-T shows a tri-exponential decay. The amplitude average decay time increases from 5.7 to 13.2 ns while monitoring the decay at the emission wavelength of 400 to 625 nm, respectively. Temperature-dependent absorption and ^{1}H NMR studies rule out any decomposition. The complex decay profile is also associated with broad and multiple emission bands. The slowest decay time (12-20 ns) is increasing with the emission wavelengths and the value is similar to that observed in different solvents at room temperature. This component is likely to be due to the emission from the ICT state. The fastest decay component (1-2 ns) remains almost constant with a decrease in the contribution from lower to higher emission wavelengths. The component with intermediate decay time (5-8 ns) can be due to the emission from the LE state mostly dominated by the donor contribution (analogous to *N*-substituted carbazole.[18]

The complex decay profiles are generally observed in viscosity and temperature dependent fluorescent probes.[19] The origin of multiexponential decay is due to the excited-state interconversions among LE, ICT and TICT states.[20] Additionally, in the present case, a possible flattening distortion

followed by stabilization through the specific interaction with solvent is also proposed as discussed below. The precise assignment of the excited state species can only be possible through in-depth analysis of the dynamics of excited-state interconversions through ultrafast spectroscopy.
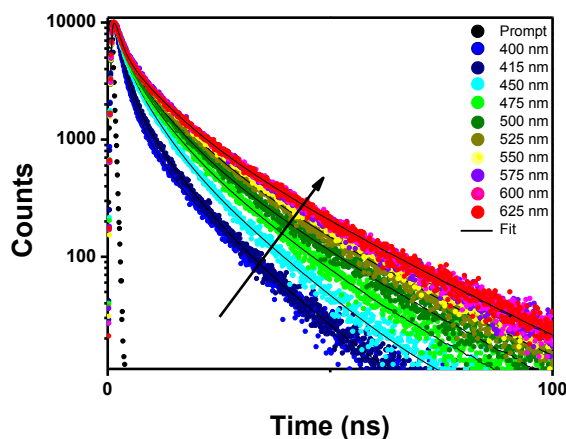

Figure S23 Fluorescence decay profiles (λ_{ex} = 339 nm) of PQCz-T in THF after cooling-heating-cooling cycle at different emission wavelengths.

Table S11 Fluorescence decay parameters of blue emitting solution after heating-cooling cycle of 5 µM PQCz-T in THF (λ_{ex} = 339) at different emission wavelengths; the decay times (τ_1, τ_2 and τ_3) and the respective fractional contributions (α_1, α_2 and α_3), the amplitude average decay time (τ_{avg}) and the quality of fitting (χ^2) are shown.

λ_{em} (nm)	Lifetime (ns)							
	τ_1	α_1	τ_2	α_2	τ_3	α_3	$\tau_{avg.}$	χ^2
400	1.1	29.2	3.4	34.5	11.8	36.3	5.7	1.06
415	1.8	40.5	6.3	36.6	14.8	21.9	6.2	1.09
450	1.3	16.6	4.9	45.7	13.4	37.6	7.4	1.12
475	1.5	17.6	5.8	42.6	15.4	39.8	8.8	1.09
500	1.3	14.3	6.3	44.5	17.5	41.2	10.2	1.10
525	1.8	15.8	7.8	45.5	20.2	37.6	11.4	1.02
550	1.8	14.8	8.1	45.2	21.1	39.9	12.3	1.09
575	1.6	13.1	8.0	44.3	21.3	42.5	12.8	1.13
600	1.3	11.4	6.8	37.0	19.9	51.5	12.9	1.16
625	1.4	12.7	7.4	37.5	20.5	49.8	13.2	1.12

5.1 The polarity effect:

The increase in temperature leads to a decrease of the permittivity (ε) and the refractive index (n) of the solvent in a nonlinear fashion and vice versa. The values of ε and n can be determined over the temperature range from the empirical formulas as given below.[21-23]

$$\varepsilon_T = \varepsilon_0(T_0) - \alpha(T - T_0) - \beta(T - T_0)^2 - \gamma(T - T_0)^3 \qquad (11)$$

$$n_T = n_0(T_0) - a(T - T_0) - b(T - T_0)^2 \qquad (12)$$

we also checked the emission behavior of PQCz-T by varying the polarity of the medium using a binary mixture of THF and hexane (Figure S24). The orange emission in THF was gradually blue shifted and a green emission was observed in 99% hexane-THF. A single emission band was observed in each fraction (Figure S25). This observation is consistent with the solvatochromic behavior of PQCz-T as demonstrated in Figure 1 in the main text. This study further ascertains that the complex spectral pattern and tunable emission from dark orange to blue including a single component white-light emission as observed in the temperature-dependent studies in THF (Figure 4 in the main text) can not be rationalized simply by the polarity effect.
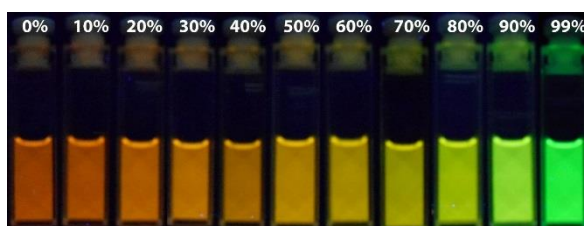
Figure S24 Photographs of PQCz-T (5 μM) in THF/hexane mixtures with increasing percentage of hexane under the illumination of UV light (λ_{ex} = 365 nm).
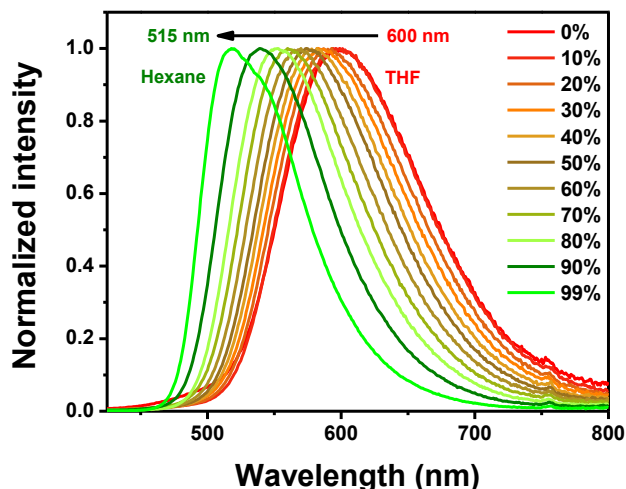
Figure S25 Emission spectra (λ_{ex} = 340 nm) of PQCz-T (5 μM) in the THF/hexane mixtures with increasing percentage of hexane.

Kuimova and coworkers unraveled the effect of temperature and polarity on photophysical properties of viscosity sensitive BODIPY-based fluorescent molecular rotors exhibiting TICT.[19, 24] We know that the viscosity and polarity would increase with the increasing fraction of glycerol.[13] We carried out a temperature dependent study of PQCz-T (5 μM) in 80% glycerol/methanol solution (218 cP, Figure S26). At lower temperature, the polarity and viscosity both have higher values and with increasing the temperature, both will decrease dramatically.[22, 23] The decrease of polarity and

viscosity is clear from the temperature dependent emission spectra of 218 cP viscous solution of PQCz-T. An intense dark red fluorescent (λ_{em} = 630 nm) solution of PQCz-T at 288 K turns orange (λ_{em} = 601 nm) with the increase of the solution temperature to 328 K. The polarity and viscosity both decreases and resulted the blue shift as well as decrease in intensity from 288 K to 328 K. Thus, we conclude that the decrease of fluorescence intensity is predominantly due to the viscosity effect whereas, the substantial blue shift of 29 nm is chiefly due to the decrease in polarity.
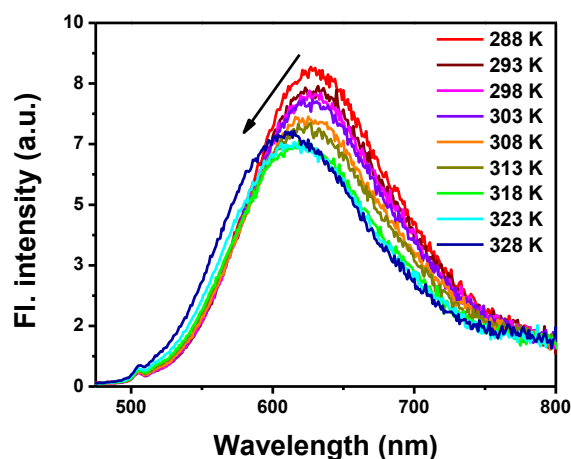
Figure S26 Emission spectra (λ_{ex} = 340 nm) of PQCz-T (5 μM) in 80% glycerol/methanol mixture (218 cP) with varying temperature.

5.2 Temperature-dependent NMR study:

In order to probe any structural change, we performed ^{1}H NMR measurements of PQCz-T in THF-d$_8$ with varying temperature. The significant downfield chemical shifts were observed for few characteristic protons in PQCz-T (d, e Figures S27 and S28) upon lowering the temperature. Subsequently, with the increase of temperature, the same protons are shielded and exhibit a progressive upfield chemical shift (Figure S28). The proton shifts could be due to the change of the polarity of the medium with temperature leading to the change in chemical as well as the magnetic environment. As discussed earlier, the solvent polarity increases with the decrease in solution temperature and *vice versa*.[22, 25, 26] However, the significant chemical shifts specifically for protons d and e cannot be accounted simply by the change in polarity. This observation suggests certain structural changes with the variation of temperature. The alteration of geometry of PQ unit with increasing temperature can change the chemical shift of adjacent protons (d, e and f). A possible structural change would be the distortion of pyrazine ring through the sp^2 N atoms leading to nonplanarity between phenanthrene and pyridine moiety in PQ (Figure S29). Such temperature-induced geometrical changes were reported in phenazine-based system.[27] In addition, the sharpening of proton signals after heating-cooling cycles also indicate the subtle change of molecular conformations.
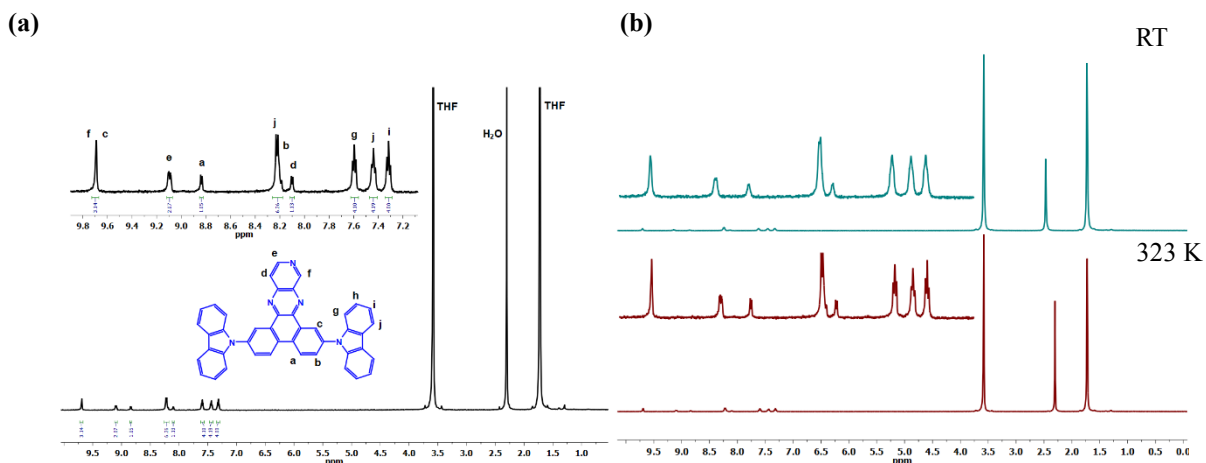
Figure S27 The ^{1}H NMR spectra of PQCz-T in (a) THF-d$_8$ at RT and (b) the same is stacked with THF-d$_8$ at 323 K (protons are assigned using 2D-NMR, Figure S46).
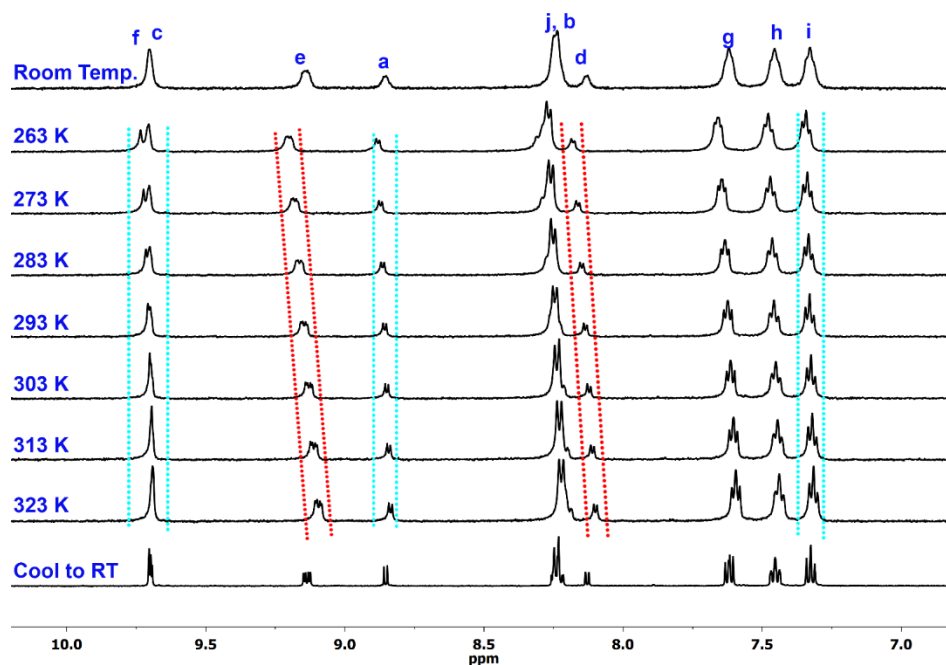

Figure S28 The chemical shift of the hydrogen of PQCz-T in THF-d$_8$ with varying the temperature (263 K to 323 K).
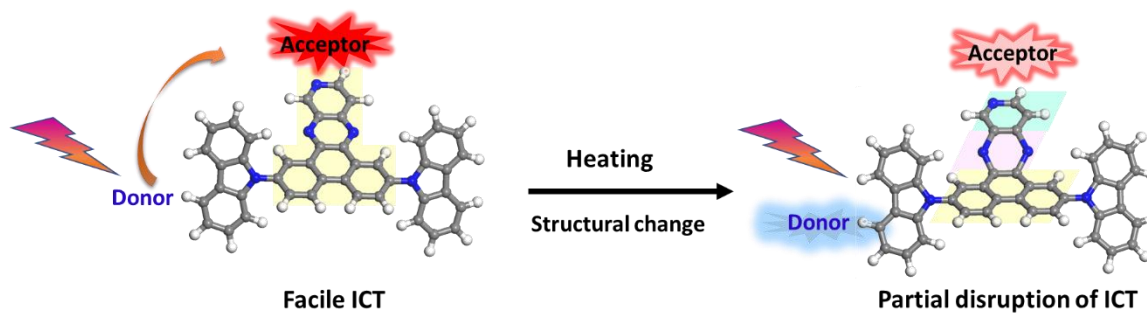

Figure S29 A possible structural change of PQCz-T with the increase of temperature.

As discussed above, the increase of solvent polarity with the decrease in temperature causes the red shift in emission. While, the decrease in solvent polarity with the increase in temperature may

account the blue shift. However, a large shift from 610 to 415 nm by changing the temperature respectively from 263 to 338 K in THF suggests some structural change apart from the polarity effect. The structural change proposed in Figure S29 may partially disrupt the ICT with the increase of the temperature and facilitates the emission also from the LE state accounting the broad and stable blue emission. The computational investigation as discussed below further indicate the specific interactions with solvent molecules.

VI. Computational investigation

The density functional theory (DFT) calculations were performed with the Gaussian 09 program package.[28-30] S_0 geometries were optimized using the B3LYP hybrid functional and 6-31G(d,p) basis set. The excited state structures were computed by employing time-dependent density functional (TD-DFT) theory with the same functional and basis sets.[1]

The spatial distributions of the highest occupied molecular orbital (HOMO) and the lowest unoccupied molecular orbital (LUMO) of PQCz-T and PQCz-V in the ground and the excited state were analyzed. In the ground state, the LUMOs of both the compounds are predominantly located on the central phenanthrene-linked pyridoquinoxaline acceptor unit (PQ), whereas the HOMOs are differently distributed (Figure 2, main text). The HOMO is mainly distributed on Cz unit in PQCz-T. On the other hand, due to the higher resonance stabilization of *p*-substituted donor, the HOMO of PQCz-V is extended to the central PQ moiety. The weak electron-donating character of phenanthrene leads to the localization of the HOMO on the phenanthrene unit along with the electron donor Cz. In the case of PQCz-T, the HOMO and the LUMO are well separated accounting to pronounce ICT characteristics. The excited state HOMO-LUMO pictures are shown in Figure S30.

The unusual temperature-induced fluorochromism in THF could be due to the specific solvent interaction with PQCz-T. We carried out a detailed systematic computational investigation to propose a model addressing the underlying phenomenon. The molecular simulations were carried out using the dielectrics of different solvents to probe the temperature induced fluorochromic behavior of PQCz-T. The ground state molecular geometry of PQCz-T was optimized employing density functional theory (DFT) B3LYP hybrid functional and 6-31G(d,p) basis set in Gaussian 09 Revision a.02 software. The TD-DFT calculation with the same functional and the basis set was employed to obtain the excited state structure. The polarizable continuum model (PCM) of solvation was used to include the solvent effects. The molecular geometries of solvents such as THF, chloroform and toluene also were first optimized using DFT. The DFT optimized structures of PQCz-T with the respective solvent molecules were chosen as model systems. The blend module in Materials Studio 6.1 was used to mix the solvent molecules with PQCz-T to evaluate the nearest neighbor packing of solvent molecules with PQCz-T. The modified Flory Huggins model and COMPASS27 force field were used to find the most stable

cluster.[31, 32] The obtained clusters were further optimized using the DMol3 module with the local-density approximation (LDA), VWN functional and DND basis set.[33-35]

A range of weak non-covalent interactions (short contacts) was realized between the excited state structure of PQCz-T and THF molecule (Figure S31). These interactions involve acidic hydrogens of THF and sp^2 nitrogens of pyridoquinoxaline in PQ unit. It is likely that the structural change of PQ units with the increasing temperature favors the binding with THF molecules through non-classical hydrogen bonding interactions. The flapping of PQ unit around two sp^2 nitrogen as shown in Figure S29 at higher temperature can create a pocket for accommodating THF molecules. In addition, the free rotation of Cz unit in PQCz-T creates the space for favorable interactions with THF. The similar extent of short contacts was not observed in the case of PQCz-V (Figure S32). As discussed earlier, the rigid molecular structure of PQCz-V is perhaps not amenable to flapping and hinder the specific interactions with solvent molecules.
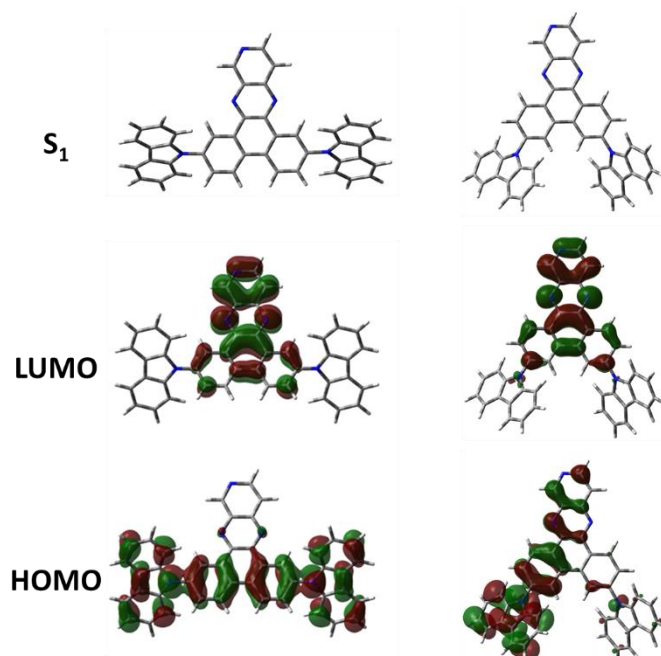
Figure S30 DFT-optimized excited-state (S_1) geometries and HOMO/LUMO distributions of PQCz-T and PQCz-V obtained by TD-DFT calculations at the B3LYP/6-31G(d,p) level.
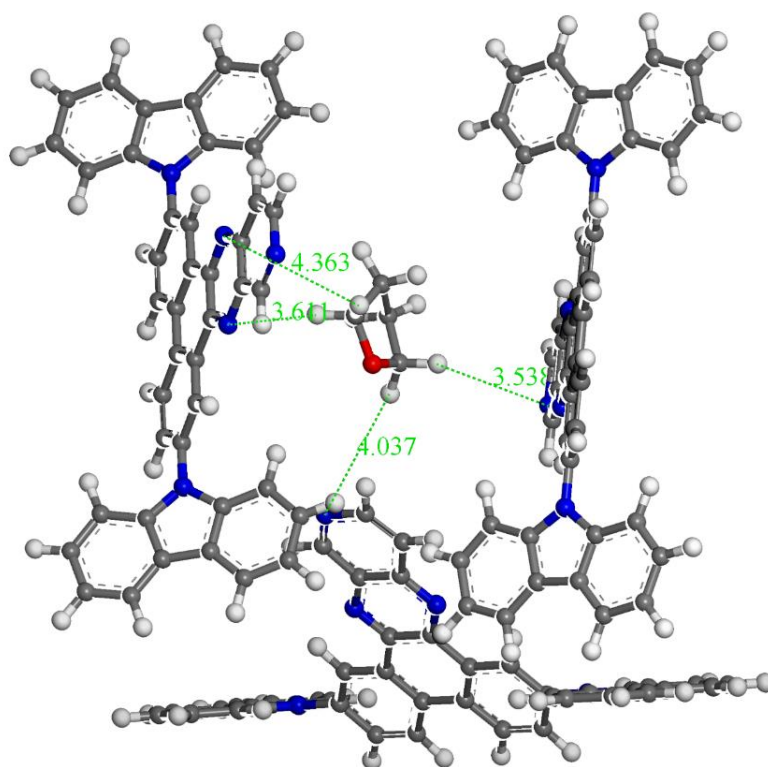
Figure S31 Cluster depicting the packing of tetrahydrofuran (THF) with excited state of PQCz-T. There are multiple number of short contacts (distances are given in Å) between the acidic proton of THF and the lone pairs of electrons on nitrogen of PQCz-T.
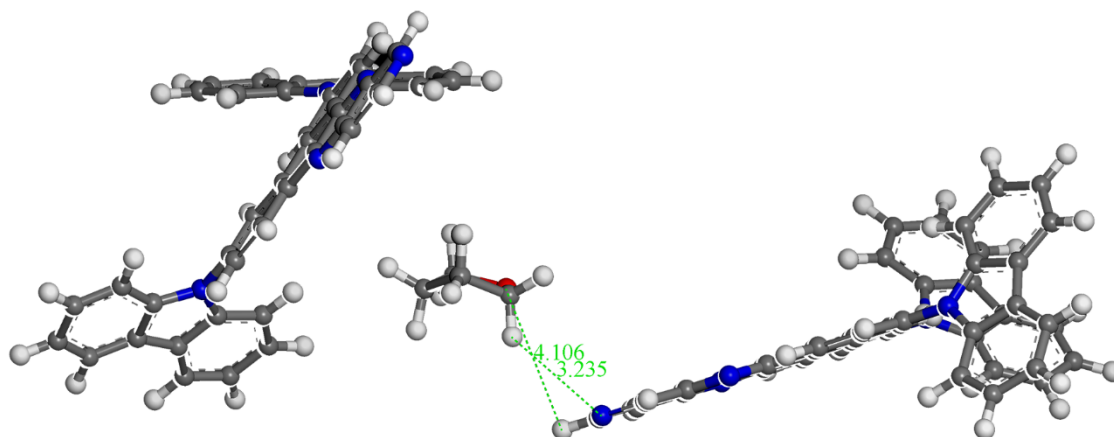

Figure S32 Cluster depicting the packing of THF with excited state of PQCz-V.

VII. Comparative table

Table S12 Comparison of PQCz-T with reported fluorescent molecular probe for multifunctional properties:

S. No.	System	Large Stokes shift	Multifunctional properties				Citation
			Red emission	Single-component white-light emission	Molecular viscometer	Molecular thermometer	
1	PQCz-T	DCM: 195 nm Toluene: 125 nm	λ_{em}(DCM): 635 nm QY: 11 % λ_{em}(Solid): 628 nm QY: 10 %	CIE: (0.36, 0.28)	425-fold increase of Fl. Intensity from 0.6 to 454 cP	610 to 415 nm from 263 to 338 K, positive T-coefficient: 0.6 % K^{-1}	*Present Paper*
2	MCBD	80 nm (yellow to red)	640 nm	-	dark red to yellow	560 to 640 nm from 84 to 280 K, 5%	*Chem. Sci.,* **2014**, *5*, 4388.[36]
3	RY	250 nm	650 nm	-	6-fold from 1.2 cP (ethanol) to 950 cP	3-fold from 25 °C to -50 °C	*J. Am. Chem. Soc.* **2011**, *133*, 6626.[37]
4	N,N-DQEA	210 nm (DMSO)	550 nm	-	-	298 to 338 K, positive T-coefficient: 0.5 % per °C	*Chem. Commun.*, **2014**, *50*, 15811.[38]
5	Porphyrin dimers	~300 nm	780 nm	-	The ratiometric enhancement (15-65 times) upon viscosity	-	*Chem. Eur. J.* **2017**, *23*, 11001.[19]
6	DAP, PP, MP, BP, EP	-	-	-	2.3-27-fold at 534 cP	37 °C to 20 °C intensity increases 2.7-3.5 times	*Chem. Commun.*, **2016**, *52*, 13695.[14]
7	BODIPY derivatives	-	-	-	20-fold from 0.6 cP to 945 cP	-	*J. Am. Chem. Soc.* **2013**, *135*, 9181.[39]
8	BODIPY derivatives	-	-	-	lifetime increases from 0.7 to 3.8 ns (28 to 950 cP)	-	*J. Am. Chem. Soc.* **2008**, *9*, 6673.[40]
9	CMAM-MCCA	-	-	-	74 mPa.s to 374 mPa.s	-	*J. Am. Chem. Soc.* **2006**, *128 (2)*, 398.[41]
10	DPTB	-	-	-	-	-50 °C to 100 °C from green to blue fluorescence with increasing QY	*Angew. Chem. Int. Ed.* **2011**, *50*, 8072.[42]
11	Caz-Cy2	-	580 nm	-	23-fold increase in intensity from 1.0 cP to 950 cP	-	*Chem. Eur. J.* **2013**, *19*, 1548.[43]
12	BN-BPh	-	565 nm	-	-	Irreversible temperature effect	*Chem. Commun.*, **2017**, *53*, 3446.[44]
13	BNAP	-	472 nm	-	Blue shift (473 to 452 nm) with increasing intensity from water to glycerol	-80 °C to 80 °C, the decrease of intensity with red shifted emission	*J. Mater. Chem. C,* **2016**, *4*, 5696.[45]

14	BDAA-methyl	5200-6700 cm^{-1}	-	-	18-times fluorescence enhancement from 4 cP-167 cP	-	*J. Am. Chem. Soc.* **2016**, *138*, 8194.[12]
15	Rhodamine derivatives		500-700 nm	-	-	2-fold decrease of fluorescence lifetime of the dye over 5−55 °C	*Anal. Chem.* **2016**, *88*, 10566.[46]
16	Mito-VH	-	607 nm	-	16-fold enhancement from pure ethanol to 95% glycerol	-	*Anal. Chem.* **2017**, *89*, 552.[47]
17	BODIPY derivatives	-	-	-	QY: 12-fold, lifetime: 18-fold, intensity: 2-fold from 1.2 cP to 1457 cP	-	*Phys. Chem. Chem. Phys.,* **2016**, *18*, 4535.[48]
18	FLAP3	-	-	-	Viscosity sensitive (2.2 to 100 cP) emission	Temperature responsive emission	*J. Mater. Chem. C,* **2017**, *5*, 5248.[49]
19	C1, C2, C3	-	-	-	-	Temperature sensitivity (dI/dT) ranging from 0.012 °C^{-1} at -50–30 °C to 0.024 °C^{-1} at 30–100 °C	*Chem. Commun.,* **2017**, *53*, 5702.[50]
20	DPTB	-	-	-	-	Positive temperature coefficient from 15-75°C	*Mater. Chem. Front.,* **2017**, *1*, 2383.[51]

VIII. FTIR spectra

The FTIR spectra of precursors and donor-acceptor molecules are shown in Figure S33. The characteristic peaks observed are: at 3040 cm^{-1} due to =C-H stretching and aromatic C-H stretching, 2950-2840 cm^{-1} -C-H stretching, 1640-1600 cm^{-1} C=C alkene and C=C (aromatic) stretching, 1480-1440 cm^{-1} C-H bending, 1360-1080 cm^{-1} C-N stretching, 750-710 cm^{-1} C-C out of plane bending and C-H (aromatic) out of plane bending.
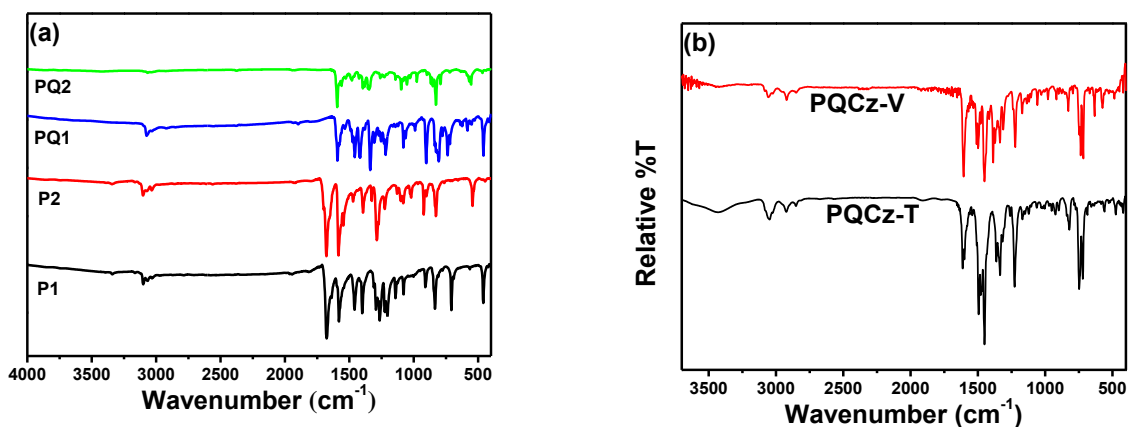

Figure S33 FTIR spectra of (a) precursors and (b) donor-acceptor molecules: PQCz-T and PQCz-V.

IX. NMR and mass spectra
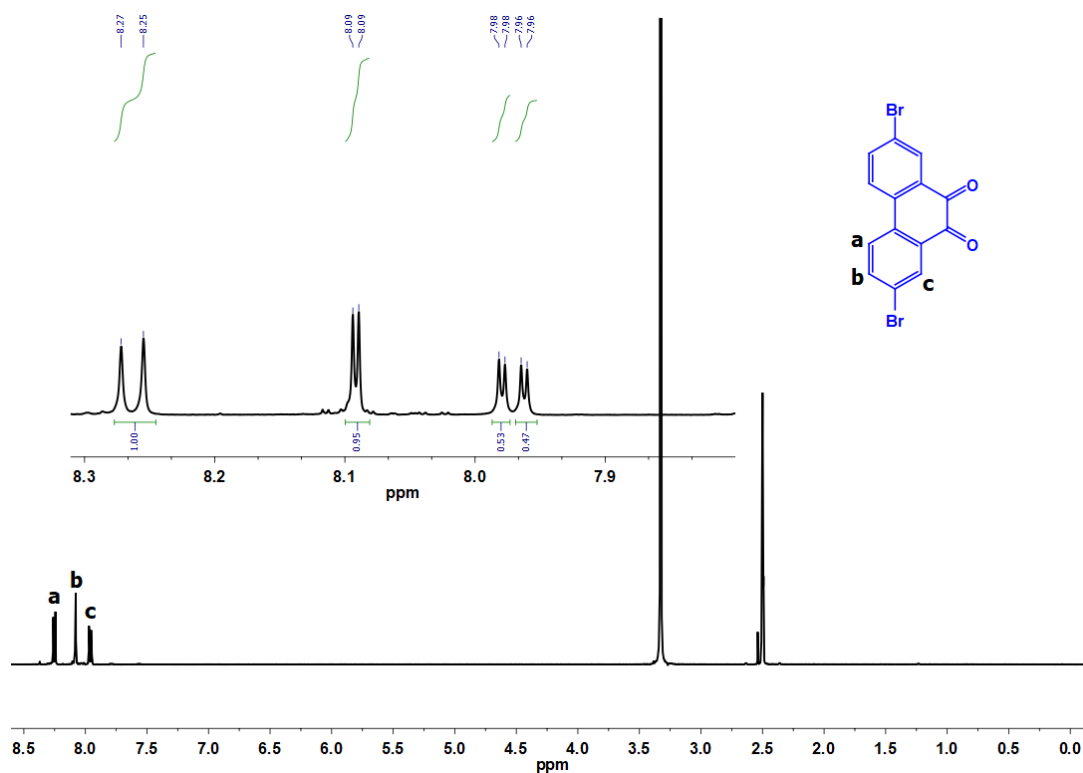
Figure S34 ^{1}H NMR spectrum of 2,7-dibromophenanthrene-9,10-quinone (P1).
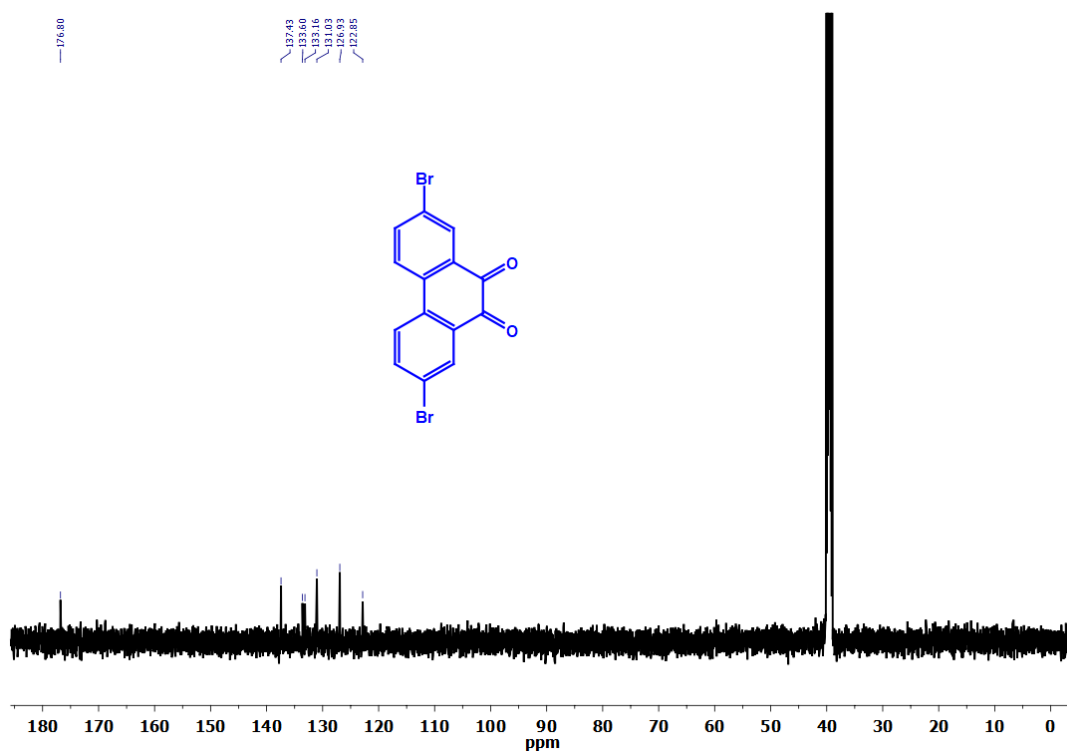
Figure S35 ^{13}C NMR spectrum of 2,7-dibromophenanthrene-9,10-quinone (P1).
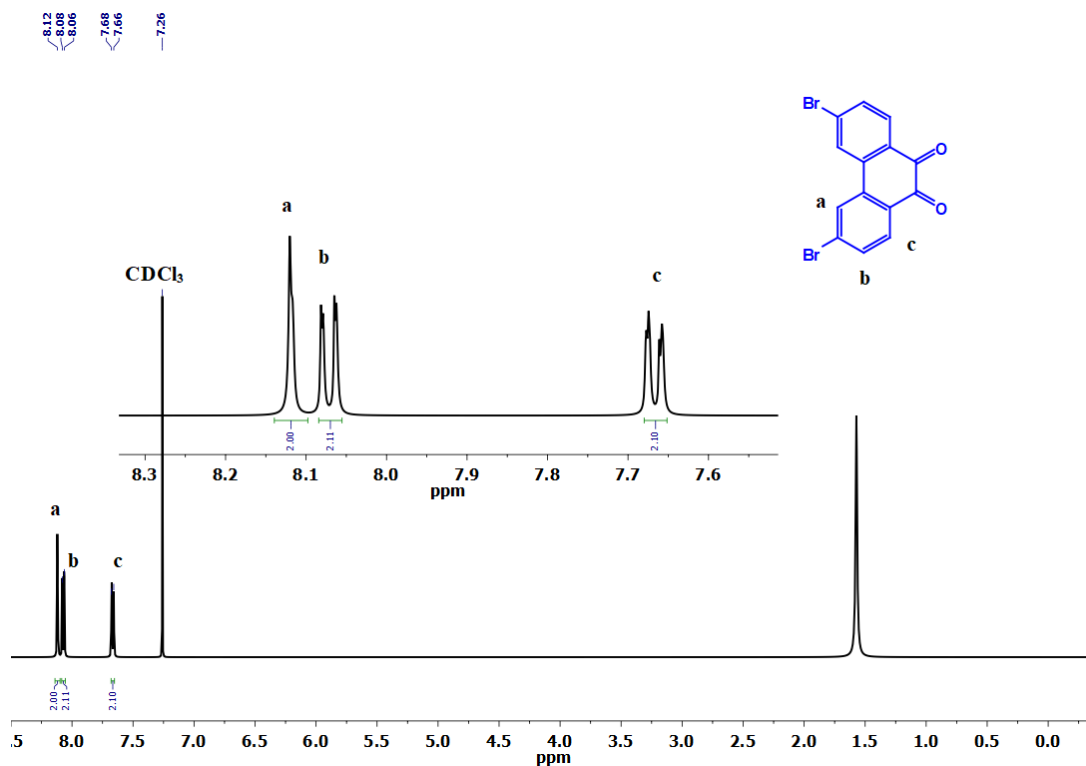
Figure S36 ^{1}H NMR spectrum of 3,6-dibromophenanthrene-9,10-quinone (P2).
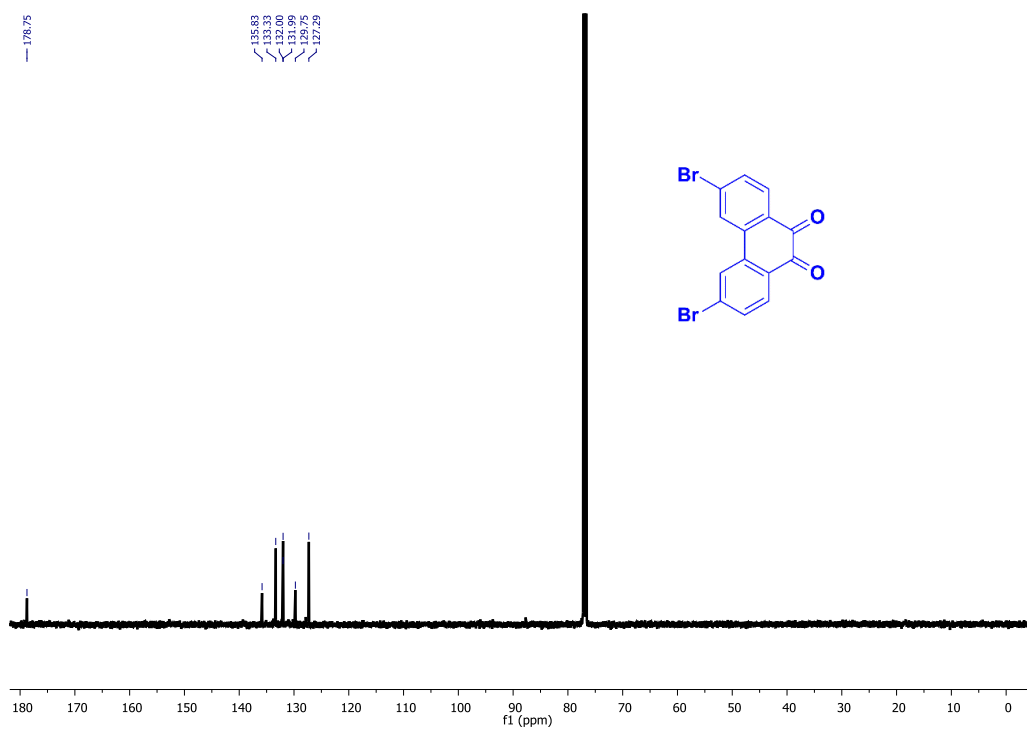
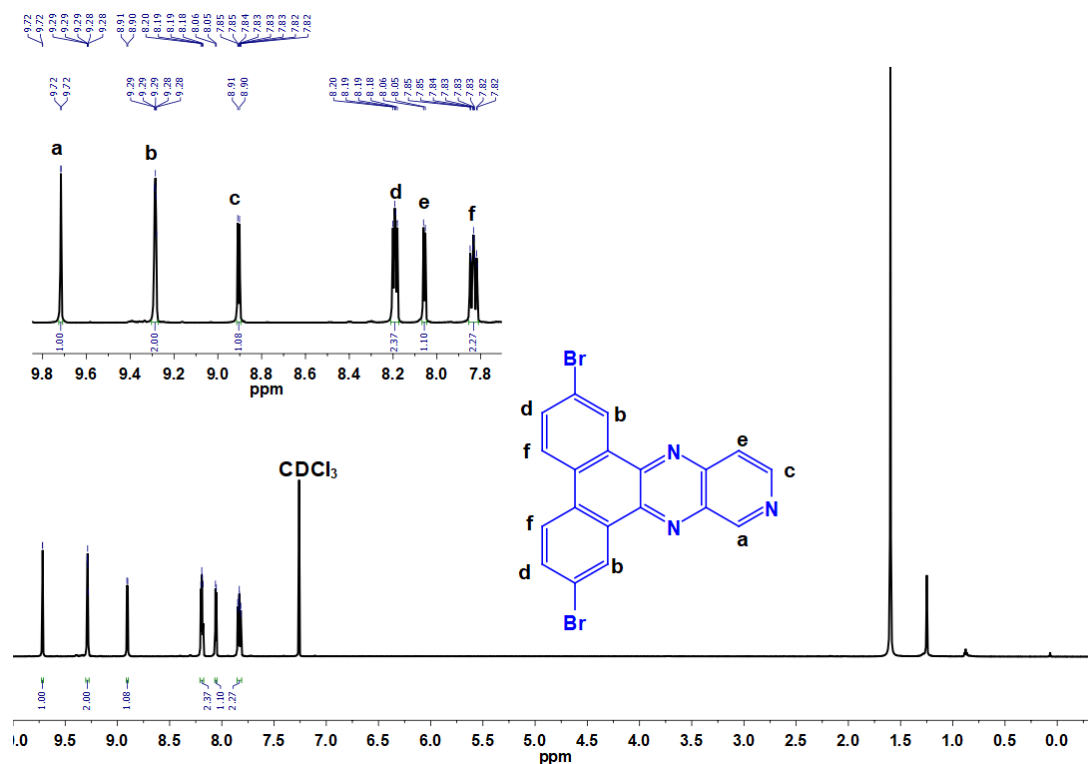**Figure S37** ^{13}C NMR spectrum of 3,6-dibromophenanthrene-9,10-quinone (P2).
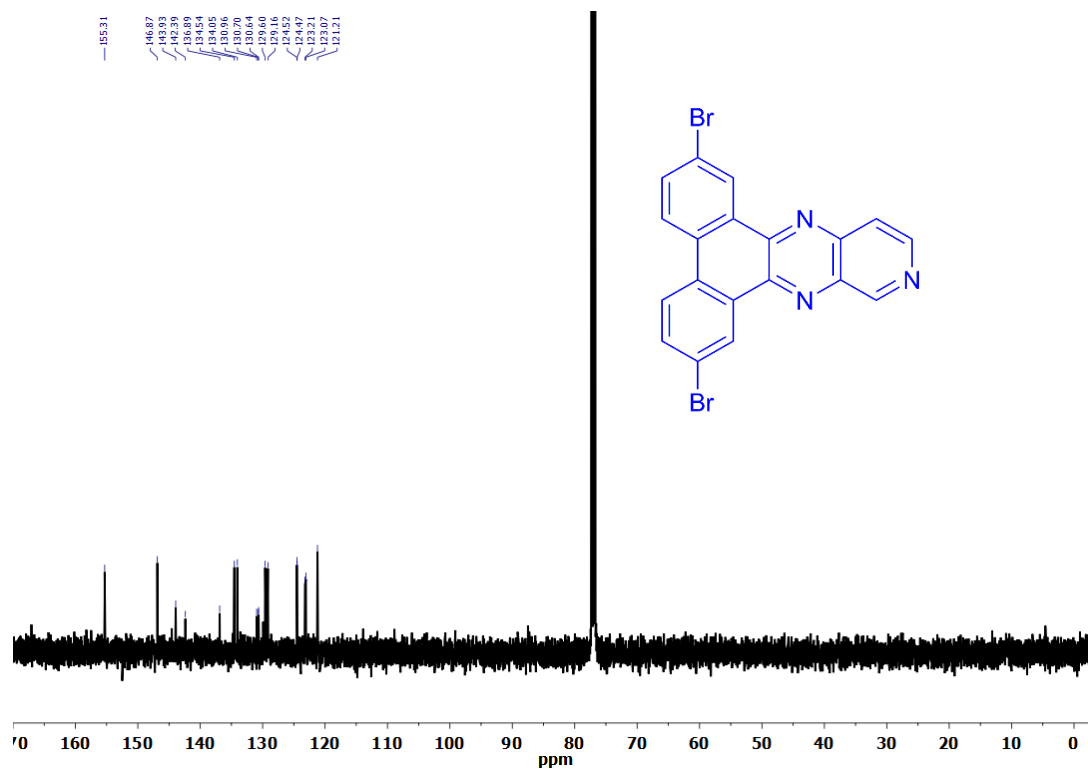
Figure S38 ^{1}H NMR spectrum of PQ1.
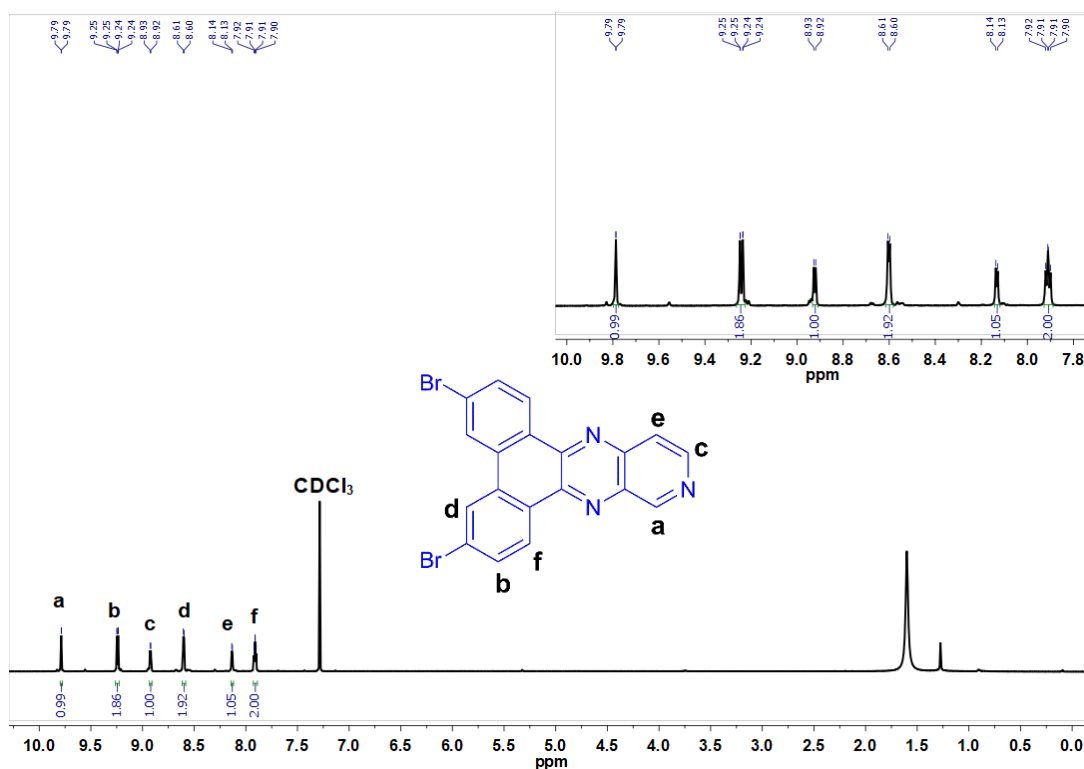

Figure S39 ^{13}C NMR spectrum of PQ1.

Figure S40 ¹H NMR spectrum of PQ2.
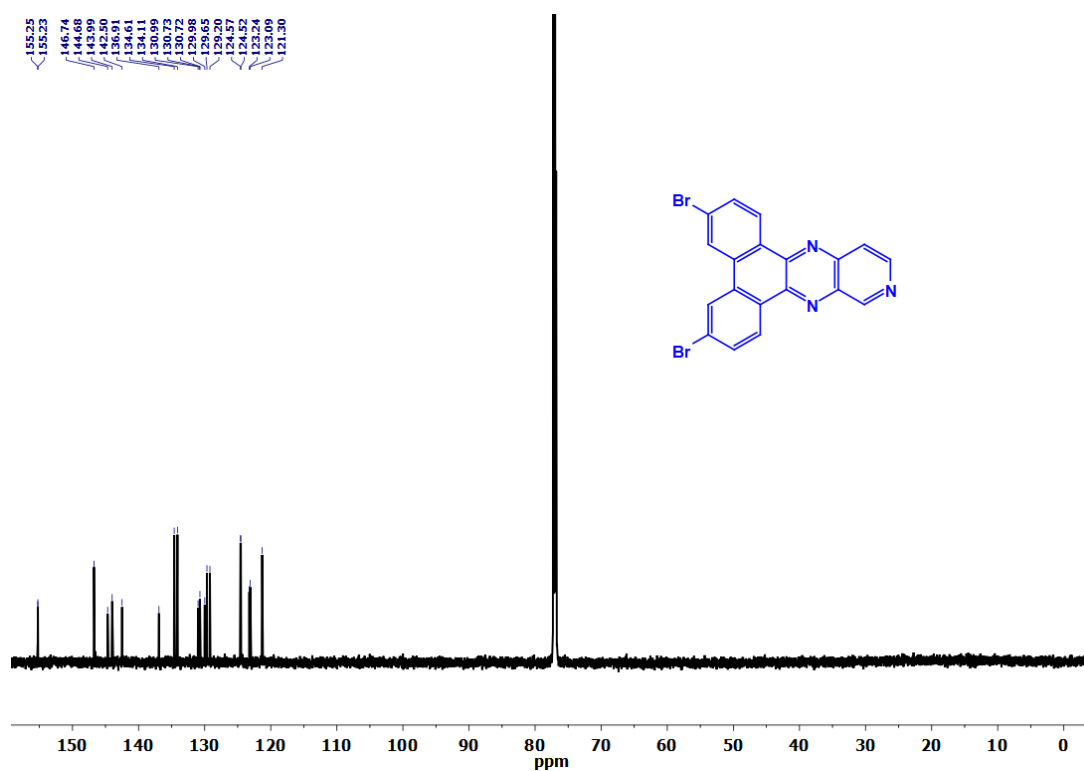
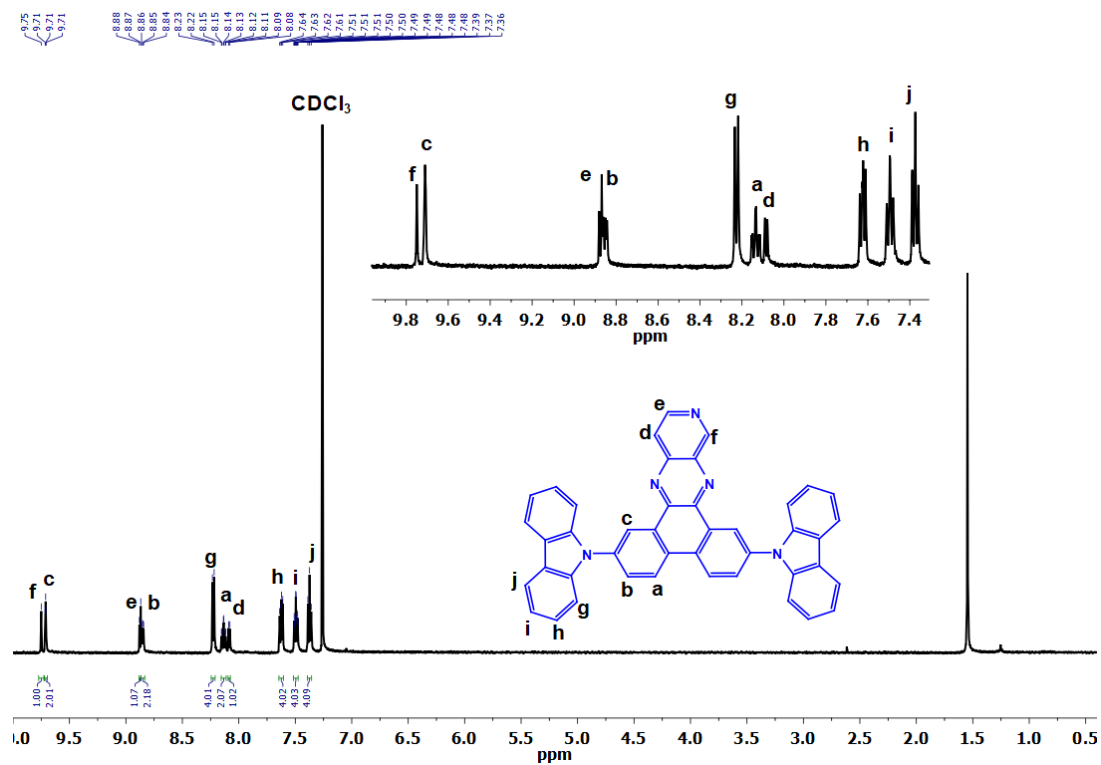**Figure S41** ¹³C NMR spectrum of PQ2.

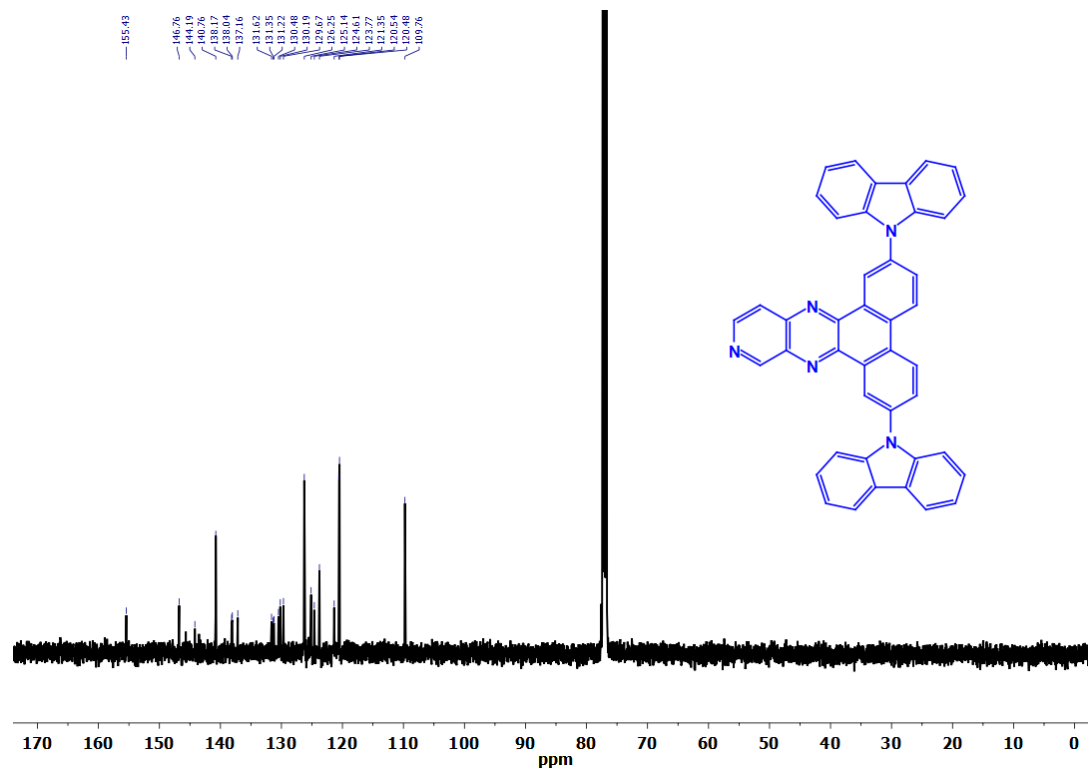**Figure S42** ^{1}H NMR spectrum of PQCz-T.
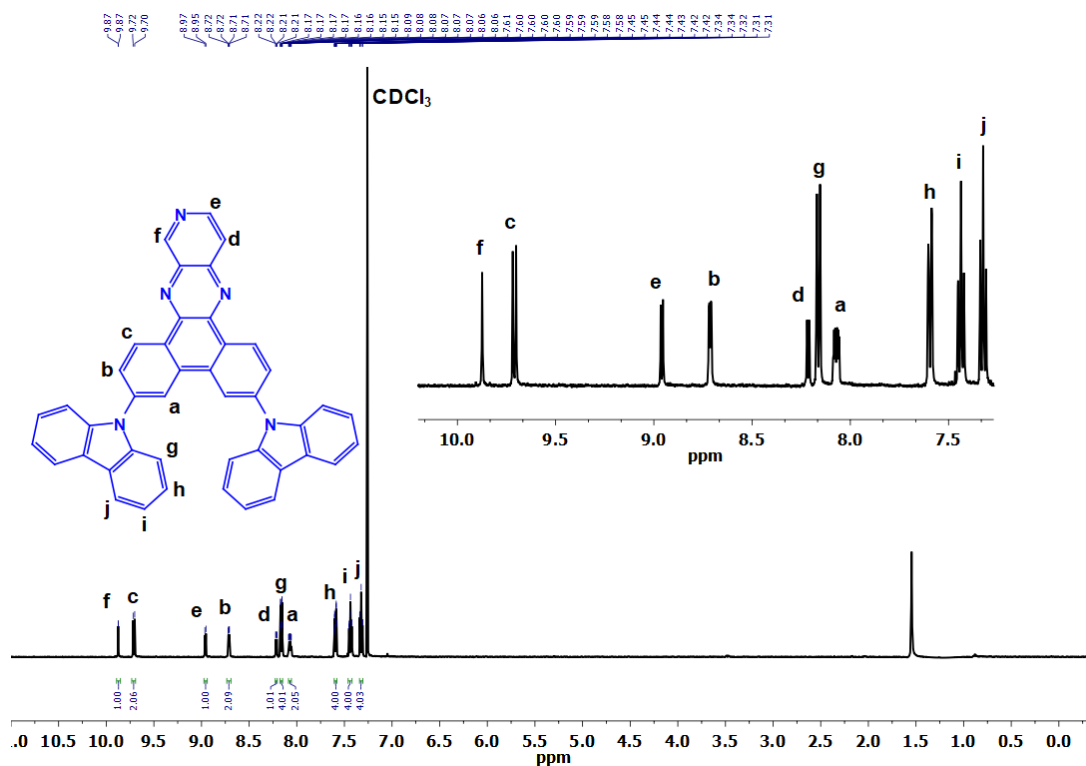

Figure S43 ^{13}C NMR spectrum of PQCz-T.

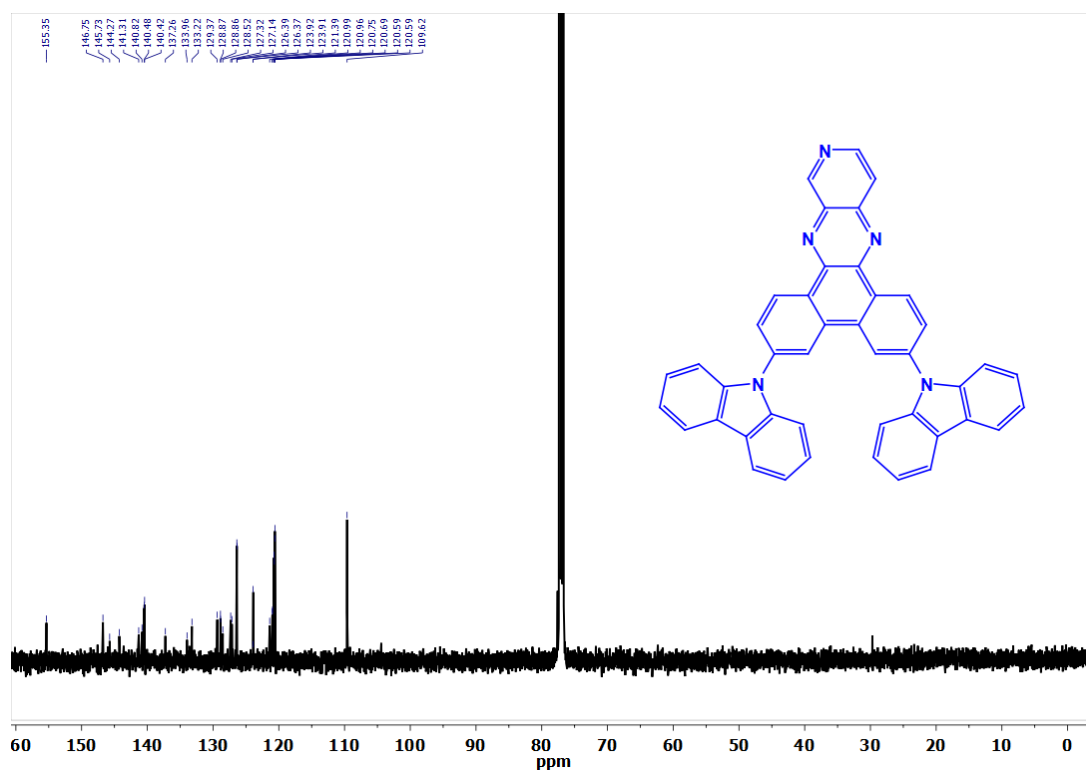**Figure S44** ^{1}H NMR spectrum of PQCz-V.

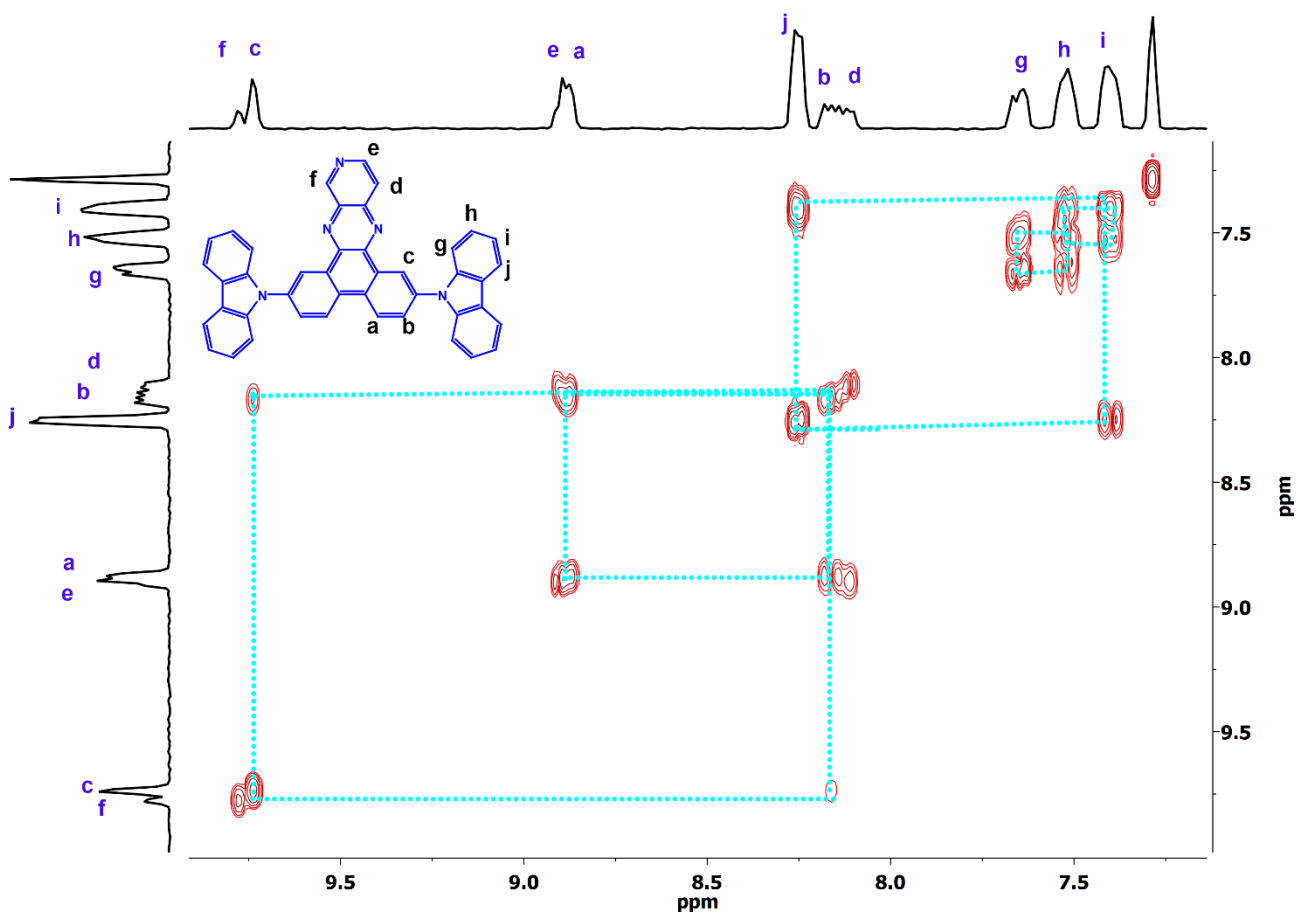**Figure S45** ^{13}C NMR spectrum of PQCz-V.

Figure S46 2D ^{1}H-^{1}H COSY NMR spectrum of PQCz-T in CDCl$_3$.

X. References

1. R. Francke and R. D. Little, *J. Am. Chem. Soc.*, 2014, **136**, 427-435.

2. B. Sk and A. Patra, *CrystEngComm*, 2016, **18**, 4290-4294.

3. S. Mukherjee, A. Chattopadhyay, A. Samanta and T. Soujanya, *J. Phys. Chem.*, 1994, **98**, 2809-2812.

4. S. Roy, P. Stollberg, R. Herbst-Irmer, D. Stalke, D. M. Andrada, G. Frenking and H. W. Roesky, *J. Am. Chem. Soc.*, 2015, **137**, 150-153.

5. F. Caruso, V. Atalla, X. G. Ren, A. Rubio, M. Scheffler and P. Rinke, *Phys. Rev. B*, 2014, **90**.

6. L. A. Estrada and D. C. Neckers, *Org. Lett.*, 2011, **13**, 3304-3307.

7. Q. S. Zhang, H. Kuwabara, W. J. Potscavage, S. P. Huang, Y. Hatae, T. Shibata and C. Adachi, *J. Am. Chem. Soc.*, 2014, **136**, 18070-18081.

8. W. J. Li, D. D. Liu, F. Z. Shen, D. G. Ma, Z. M. Wang, T. Feng, Y. X. Xu, B. Yang and Y. G. Ma, *Adv. Funct. Mater.*, 2012, **22**, 2797-2803.

9. C. Reichardt, *Chem. Rev.*, 1994, **94**, 2319-2358.

10. K. Rurack and M. Spieles, *Anal. Chem.*, 2011, **83**, 1232-1242.

11. C. Wurth, M. Grabolle, J. Pauli, M. Spieles and U. Resch-Genger, *Nat. Protoc.*, 2013, **8**, 1535-1550.

12. S. Sasaki, S. Suzuki, W. M. C. Sameera, K. Igawa, K. Morokuma and G. Konishi, *J. Am. Chem. Soc.*, 2016, **138**, 8194-8206.

13. J. A. Levitt, P. H. Chung, M. K. Kuimova, G. Yahioglu, Y. Wang, J. L. Qu and K. Suhling, *ChemPhysChem*, 2011, **12**, 662-672.

14. S. C. Lee, J. Heo, J. W. Ryu, C. L. Lee, S. Kim, J. S. Tae, B. O. Rhee, S. W. Kim and O. P. Kwon, *Chem. Commun.*, 2016, **52**, 13695-13698.

15. J. R. Lakowicz, *Principles of fluorescence spectroscopy*, Springer, New York, 2006.

16. S. Ghosh, A. Roy, D. Banik, N. Kundu, J. Kuchlyan, A. Dhir and N. Sarkar, *Langmuir*, 2015, **31**, 2310-2320.

17. J. S. Lee, R. B. M. Koehorst, H. van Amerongen and J. Feijen, *J. Phys. Chem. B*, 2011, **115**, 13162-13167.

18. S. M. Bonesi and R. Erra-Balsells, *J. Lumin.*, 2001, **93**, 51-74.

19. A. Vysniauskas, D. Ding, M. Qurashi, I. Boczarow, M. Balaz, H. L. Anderson and M. K. Kuimova, *Chem. Eur. J.*, 2017, **23**, 11001.

20. M. Mao, M. G. Ren and Q. H. Song, *Chem. Eur. J.*, 2012, **18**, 15512-15522.

21. M. Mac, A. Danel, A. Michno and R. Krolicki, *J. Lumin.*, 2006, **121**, 39-50.

22. A. Kawski, B. Kuklinski and P. Bojarski, *Chem. Phys. Lett.*, 2008, **455**, 52-54.

23. R. R. Hu, E. Lager, A. Aguilar-Aguilar, J. Z. Liu, J. W. Y. Lam, H. H. Y. Sung, I. D. Williams, Y. C. Zhong, K. S. Wong, E. Pena-Cabrera and B. Z. Tang, *J. Phys. Chem. C*, 2009, **113**, 15845-15853.

24. A. Vysniauskas, M. Qurashi, N. Gallop, M. Balaz, H. L. Anderson and M. K. Kuimova, *Chem. Sci.*, 2015, **6**, 5773-5778.

25. I. Gryczyński and A. Kawski, *Z. Naturforsch. A*, 1975, **30**, 287.

26. J. Catalan, *Phys. Chem. Chem. Phys.*, 2015, **17**, 12515-12520.

27. J. W. Chen, Y. S. Wu, X. D. Wang, Z. Y. Yu, H. Tian, J. N. Yao and H. B. Fu, *Phys. Chem. Chem. Phys.*, 2015, **17**, 27658-27664.

28. A. D. Becke, *J. Chem. Phys.*, 1993, **98**, 5648-5652.

29. C. Lee, W. Yang and R. G. Parr, *Phys. Rev. B*, 1988, **37**, 785-789.

30. B. Miehlich, A. Savin, H. Stoll and H. Preuss, *Chem. Phys. Lett.*, 1989, **157**, 200-206.

31. P. J. Flory, *Principles of polymer chemistry*, Ithaca : Cornell University Press, 1953., 1953.

32. K. S. Schweizer, *J. Chem. Phys.*, 1989, **91**, 5802-5821.

33. A. Deshmukh, S. Bandyopadhyay, A. James and A. Patra, *J. Mater. Chem. C*, 2016, **4**, 4427-4433.

34. K. Pajula, M. Taskinen, V. P. Lehto, J. Ketolainen and O. Korhonen, *Mol. Pharmaceut.*, 2010, **7**, 795-804.

35. J. Gupta, C. Nunes, S. Vyas and S. Jonnalagadda, *J. Phys. Chem. B*, 2011, **115**, 2014-2023.

36. Y. X. Guo, S. Z. Gu, X. Feng, J. N. Wang, H. W. Li, T. Y. Han, Y. P. Dong, X. Jiang, T. D. James and B. Wang, *Chem. Sci.*, 2014, **5**, 4388-4393.

37. X. J. Peng, Z. G. Yang, J. Y. Wang, J. L. Fan, Y. X. He, F. L. Song, B. S. Wang, S. G. Sun, J. L. Qu, J. Qi and M. Yang, *J. Am. Chem. Soc.*, 2011, **133**, 6626-6635.

38. C. Cao, X. Liu, Q. Qiao, M. Zhao, W. Yin, D. Mao, H. Zhang and Z. Xu, *Chem. Commun.*, 2014, **50**, 15811-15814.

39. Z. Yang, Y. He, J. H. Lee, N. Park, M. Suh, W. S. Chae, J. F. Cao, X. J. Peng, H. Jung, C. Kang and J. S. Kim, *J. Am. Chem. Soc.*, 2013, **135**, 9181-9185.

40. M. K. Kuimova, G. Yahioglu, J. A. Levitt and K. Suhling, *J. Am. Chem. Soc.*, 2008, **130**, 6672-6673.

41. M. A. Haidekker, T. P. Brady, D. Lichlyter and E. A. Theodorakis, *J. Am. Chem. Soc.*, 2006, **128**, 398-399.

42. J. Feng, K. J. Tian, D. H. Hu, S. Q. Wang, S. Y. Li, Y. Zeng, Y. Li and G. Q. Yang, *Angew. Chem. Int. Ed.*, 2011, **50**, 8072-8076.

43. F. Liu, T. Wu, J. F. Cao, S. Cui, Z. G. Yang, X. X. Qiang, S. G. Sun, F. L. Song, J. L. Fan, J. Y. Wang and X. J. Peng, *Chem. Eur. J.*, 2013, **19**, 1548-1553.

44. S. Y. Li, Y. J. Hui, Z. B. Sun and C. H. Zhao, *Chem. Commun.*, 2017, **53**, 3446-3449.

45. T. K. Xia, L. L. Wang, Y. Qu, Y. C. Rui, J. Cao, Y. Hu, J. Yang, J. W. Wu and J. L. Xu, *J. Mater. Chem. C*, 2016, **4**, 5696-5701.

46. J. Jenkins, S. M. Borisov, D. B. Papkovsky and R. I. Dmitriev, *Anal. Chem.*, 2016, **88**, 10566-10572.

47. M. G. Ren, B. B. Deng, K. Zhou, X. Q. Kong, J. Y. Wang and W. Y. Lin, *Anal. Chem.*, 2017, **89**, 552-555.

48. S. L. Raut, J. D. Kimball, R. Fudala, I. Bora, R. Chib, H. Jaafari, M. K. Castillo, N. W. Smith, I. Gryczynski, S. V. Dzyuba and Z. Gryczynski, *Phys. Chem. Chem. Phys.*, 2016, **18**, 4535-4540.

49. R. Kotani, H. Sotome, H. Okajima, S. Yokoyama, Y. Nakaike, A. Kashiwagi, C. Mori, Y. Nakada, S. Yamaguchi, A. Osuka, A. Sakamoto, H. Miyasaka and S. Saito, *J. Mater. Chem. C*, 2017, **5**, 5248-5256.

50. Q. Fang, J. Li, S. Li, R. Duan, S. Wang, Y. Yi, X. Guo, Y. Qian, W. Huang and G. Yang, *Chem. Commun.*, 2017, **53**, 5702-5705.

51. W. Chi, W. Yin, Q. Qi, Q. Qiao, Y. Lin, Z. Zhu, S. Vijayan, M. Hashimoto, G. Udayakumar, Z. Xu and X. Liu, *Mater. Chem. Front.*, 2017, **1**, 2383-2390.